JCB Journal of Cell Biology

ARTICLE

Molecular organization of cytokinesis node predicts the constriction rate of the contractile ring

Kimberly Bellingham-Johnstun, Erica Casey Anders, John Ravi, Christina Bruinsma, and Caroline Laplante

The molecular organization of cytokinesis proteins governs contractile ring function. We used single molecule localization microscopy in live cells to elucidate the molecular organization of cytokinesis proteins and relate it to the constriction rate of the contractile ring. Wild-type fission yeast cells assemble contractile rings by the coalescence of cortical proteins complexes called nodes whereas cells without Anillin/Mid1p (*Δmid1*) lack visible nodes yet assemble contractile rings competent for constriction from the looping of strands. We leveraged the *Δmid1* contractile ring assembly mechanism to determine how two distinct molecular organizations, nodes versus strands, can yield functional contractile rings. Contrary to previous interpretations, nodes assemble in *Δmid1* cells. Our results suggest that Myo2p heads condense upon interaction with actin filaments and an excess number of Myo2p heads bound to actin filaments hinders constriction thus reducing the constriction rate. Our work establishes a predictive correlation between the molecular organization of nodes and the behavior of the contractile ring.

Introduction

Cell division by the constriction of a ring of actin and myosin is highly conserved from yeast to mammals. How proteins organize within the contractile ring likely governs the mechanisms of constriction. Many proteins are involved in cytokinesis, but despite a wealth of information regarding their concentration, localization, and timing of recruitment to the contractile ring, their molecular organization within the contractile ring remains relatively unknown (Pollard, 2017).

Fission yeast remains a leading model for studying cell division due to the large number of well-characterized cytokinesis proteins and the ease of genetic manipulation. Throughout the cell cycle of fission yeast, many proteins that regulate cytokinesis or build the contractile ring localize to cortical protein complexes called nodes (Moseley et al., 2009; Saha and Pollard, 2012a; Wu et al., 2006). Two types of interphase nodes, type 1 and type 2, interact, leading to the formation of a band of cortical cytokinesis nodes distributed around the equator of the cell, the presumptive division plane (Akamatsu et al., 2014; Deng and Moseley, 2013). The cytokinesis node proteins including the myosin-II molecule Myo2 (composed of the heavy chain Myo2p and light chains Rlc1p and Cdc4p), IQGAP (IQ motif containing GTPase-activating protein)-homologue Rng2p, F-BAR (Fes/CIP4 homology-Bin/amphiphysin/Rvs) protein Cdc15p, and formin Cdc12p are recruited to nodes in a sequential and timely manner, culminating with the arrival of Cdc12p (Wu et al., 2003; Wu et al., 2006). The arrival of Cdc12p to nodes coincides with the polymerization of actin filaments and the coalescense of the nodes into a contractile ring via a search, capture, pull, and release mechanism (Vavylonis et al., 2008).

Anillins contribute to cytokinesis across many species as scaffolding proteins connecting different components of the contractile ring or linking proteins of the contractile ring to regulators of the cell cycle (Piekny and Maddox, 2010). Mid1p shares structural similarities with anillins of other species, albeit with moderately conserved protein sequences (Chatterjee and Pollard, 2019; Sun et al., 2015). Mid1p localizes to type 1 interphase nodes early in G2 and joins the type 2 interphase nodes ∼30 min before spindle pole body (SPB) separation (Akamatsu et al., 2014; Guzman-Vendrell et al., 2013). During mitosis, Mid1p localizes to cytokinesis nodes. Mid1p leaves the contractile ring before the onset of constriction (Wu et al., 2006).

Cells lacking Mid1p (*Δmid1*) are viable but exhibit delayed contractile ring assembly, exhibit misplaced and oblique contractile rings and septa, and are branched and multiseptated (Paoletti and Chang, 2000; Saha and Pollard, 2012a; Sohrmann et al., 1996). Unlike wild-type cells, *Δmid1* cells do not assemble the typical band of discrete cytokinesis nodes around their equator. Instead, *Δmid1* cells assemble their contractile ring by the looping of strands composed of cytokinesis proteins. Together, those observations support the interpretation that Mid1p

Molecular Biomedical Sciences Department, College of Veterinary Medicine, North Carolina State University, Raleigh, NC.

Correspondence to Caroline Laplante: claplan@ncsu.edu.

is responsible for the organization of cytokinesis proteins into nodes. Yet both interphase nodes and Cdc12p in cytokinesis nodes are detected in *Δmid1* cells (Akamatsu et al., 2014; Saha and Pollard, 2012a). Nodes are detected in the constricting contractile ring, after the departure of Mid1p, when live cells are imaged using high-speed single-molecule localization microscopy (SMLM; Laplante et al., 2016b). Despite their multiple cytokinesis defects, *Δmid1* cells assemble contractile rings competent for constriction, raising an important question: What is the molecular organization of cytokinesis proteins in the absence of Mid1p?

Here, we use high-speed SMLM in live fission yeast cells to determine the organization of Myo2p, Rng2p, Cdc15p, and Cdc12p in the strands and contractile rings of *Δmid1* cells. We observed nodes in all strands and contractile rings of *Δmid1* cells, indicating that Mid1p is dispensable for the organization of cytokinesis proteins into nodes. We identified two different types of strands in *Δmid1* cells, nascent and enduring strands. While the general organization of cytokinesis proteins within nodes remains constant across both types of strands, the Myo2p motor-heads spread differently between nascent and enduring strands. The presence of actin filaments and the acetylation of tropomyosin cause the compaction of Myo2p motor-heads in nodes. Importantly, each type of strand generates contractile rings with distinct constriction rates. We find that the distribution of Myo2p motor-heads in the nodes of strands strongly correlates with the constriction rate of the contractile ring it generates. This work establishes a relationship between the molecular organization of cytokinesis nodes and the behavior of the contractile ring.

Results

Nascent and enduring strands in *Δmid1* cells build contractile rings that constrict with distinct rates

In preparation for cytokinesis, wild-type fission yeast cells assemble a contractile ring from the coalescence of a band of nodes (Wu et al., 2003). In contrast, *Δmid1* cells assemble rings from the looping of strands (Fig. 1, A and B). We observed two distinct types of strands in *Δmid1* cells that we named nascent and enduring. Both types of strands differ in their morphology, in the timing of their appearance, and in the timing of their looping into contractile rings. Nascent strands appear at the site of cell division shortly after SPB separation (Fig. 1 B). They form as a network of fine filaments emanating from a localized cortical source and are composed of actin filaments and cytokinesis proteins. Enduring strands are long bundles of actin filaments and cytokinesis proteins typically oriented along the long axis of the cell. They are present in cells with two separated SPBs, suggesting that cells with enduring strands have completed anaphase but not cytokinesis (Fig. 1, A and B). In the rare cases that we witnessed the birth of enduring strands, they assembled either from a nascent strand that failed to make a contractile ring or from a disassembling contractile ring at the end of constriction. About half of the cells that have an enduring strand at the start of a 2-h time-lapse acquisition form a contractile ring during the imaging. Contractile rings made from either type of strands are competent for constriction and often assemble off-center, resulting in asymmetric cell division (Bähler et al., 1998a; Paoletti and Chang, 2000; Saha and Pollard, 2012a; Sohrmann et al., 1996; Wu et al., 2006).

We used the separation of the SPBs to time the assembly of a contractile ring from nascent strands in *Δmid1* cells (Wu et al., 2003). As the assembly of enduring strands is not linked to SPB separation, we do not compare the timing of cytokinesis events for contractile rings assembled from enduring strands with those assembled from nascent strands or a band of nodes (Fig. 1, C and D). In wild-type cells, nodes labeled with monomeric EGFP (mEGFP)–Myo2p appear at the equator of the cell at −10, i.e., 10 min before SPB separation (Fig. 1, B and C). Nodes then coalesce into a contractile ring by +21 min, and contractile rings begin to constrict at +36 min (Fig. 1, B and D). In contrast, nascent strands in *Δmid1* cells labeled with mEGFP-Myo2p appear at +5 min, a 15-min delay compared with wild-type cells. The nascent strands condense into a contractile ring at +27 min after their appearance at the division plane, and the resulting contractile rings start to constrict at +33 min, comparable with wild-type.

The type of strand that builds the contractile ring may affect its mechanics, including its rate of constriction. The rate of contractile ring constriction in wild-type cells is 0.27 µm/min (Fig. 1, E and F; Laplante et al., 2015). The average constriction rate of *Δmid1* contractile rings is 0.27 µm/min (Saha and Pollard, 2012a), but the distribution of constriction rates appears bimodal with fast and slow subpopulations. The type of strand that builds the contractile ring strongly correlates with its constriction rate, with contractile rings made from nascent strands constricting faster (0.32 µm/min) and contractile rings made from enduring strands constricting more slowly (0.20 µm/min; Fig. 1 E).

We considered that the two types of strands could result from differences in genetic backgrounds due to the accumulation of random suppressor mutations in *Δmid1* cells. We imaged *mid1-366* Rlc1p-tdTomato Sad1p-mEGFP cells preincubated at nonpermissive temperature and observed contractile ring assembly from both nascent and enduring strands. Contractile rings made by nascent strands constricted at 0.35 µm/min, whereas those made by enduring strands constricted at 0.22 µm/min (Fig. S1 A). Interestingly, *mid1-366* Rlc1p-tdTomato Sad1p-mEGFP cells grown at room temperature assemble contractile rings either by the coalescence of a band of equatorial nodes (~80%; $n = 46$ cells) or from the looping of a nascent strand (~20%). Therefore, nascent and enduring strands are the results of defective Mid1p function.

The different constriction rates between contractile rings made from nascent versus enduring strands could be caused by a difference in their protein composition. We used quantitative confocal microscopy to measure the number of mEGFP-labeled Cdc12p, Cdc15p, Rng2p, Myo2p, and Myp2p in the contractile rings of wild-type and *Δmid1* cells (Wu et al., 2008; Wu and Pollard, 2005). We measured the number of cytokinesis protein per length of contractile ring for contractile rings of different sizes. Except for Myo2p and Myp2p, we observed comparable trends in protein numbers of contractile rings in

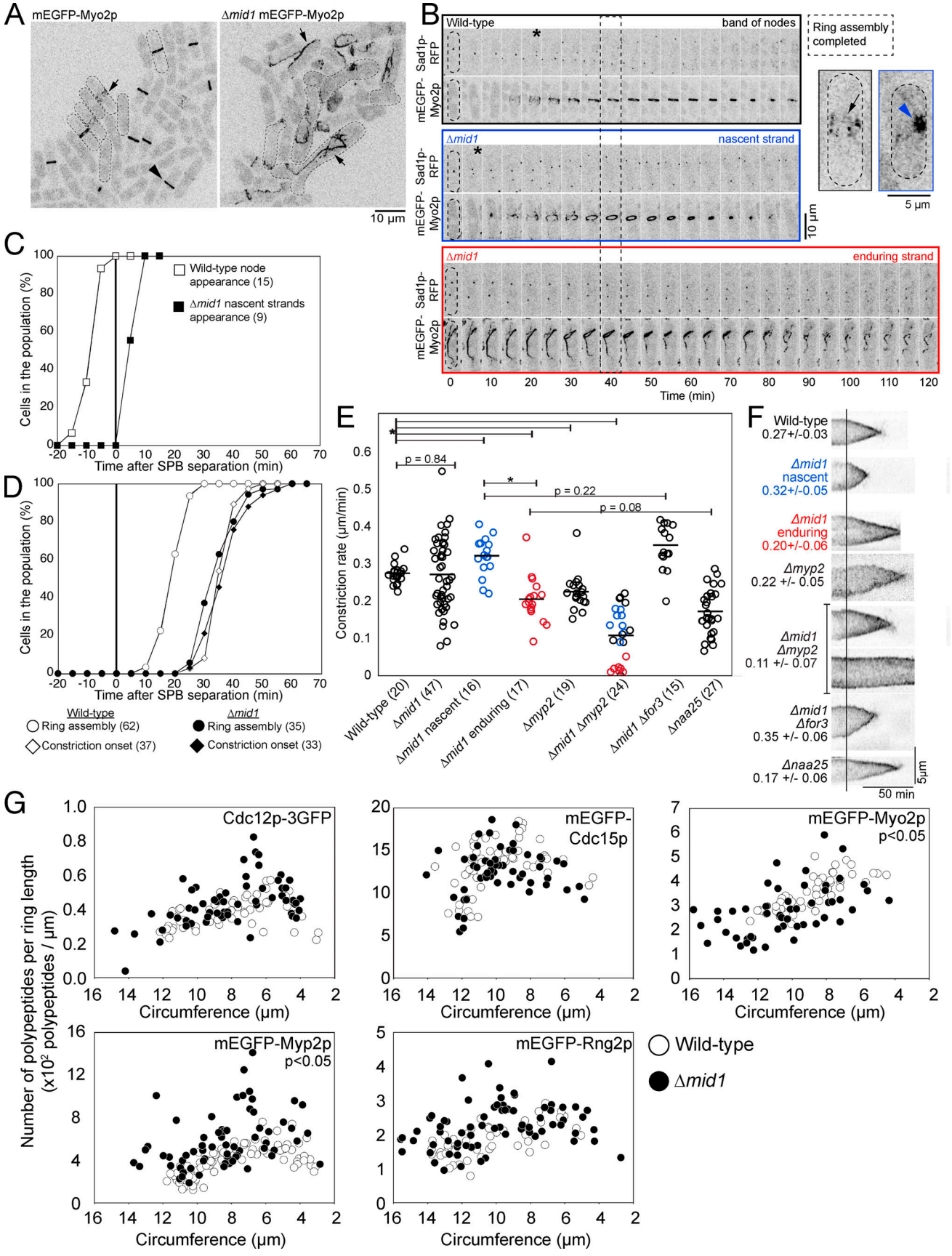

Figure 1. **Timing of cytokinesis and contractile ring constriction rate differ in *Δmid1* cells. (A)** Confocal fluorescence micrographs of fields of cells. Arrow points to a band of nodes in a wild-type cell (left) and to strands in *Δmid1* cells (right). Arrowhead points to a contractile ring in wild-type cell (left). **(B)** Time

series of micrographs of strains expressing mEGFP-Myo2p in wild-type (top) or *Δmid1* (middle and bottom). Cells are aligned at the time of completion of contractile ring assembly. Close-ups of wild-type (left) and *Δmid1* (right) cells. Black arrow, band of nodes. Blue arrowhead, nascent strand. Asterisks, SPB separation. **(C)** Outcomes plot showing the appearance of nodes or strands over time. **(D)** Outcomes plot showing the accumulation of assembled rings or constricting rings over time in the cell population. **(E)** Swarm plot of the constriction rate for individual cells. Bar, mean. Number of cells counted in brackets. Statistical significance (asterisks) determined by two-sided Student's *t* test; $P < 0.05$. Data distribution was assumed to be normal, but this was not formally tested. **(F)** Kymographs at 1-min intervals for contractile ring in horizontally oriented single cells generated from time series of micrographs. Kymographs are aligned on the vertical line at the time of ring constriction onset. Numbers, mean ± SD. **(G)** Plots of the distribution of the number of polypeptides per ring length for five cytokinesis proteins. Statistical significance determined by KS test; $P < 0.05$. RFP, red fluorescent protein.

both wild-type and *Δmid1* cells, albeit with a greater measured variability in *Δmid1* cells (Fig. 1 G). Some contractile rings in *Δmid1* cells accumulate more myosin-II Myp2p, which could explain the different constriction rate (Laplante et al., 2015). We generated *Δmid1 Δmyp2* double-mutant cells and found that the distribution of constriction rates of their contractile rings is still bimodal, albeit with both populations constricting 25–50% more slowly than the *Δmid1* populations, consistent with Myp2p being responsible for ∼50% of the constriction rate (Fig. 1, E and F; Laplante et al., 2015). Thus, *Δmid1* cells assemble contractile rings that constrict with either of two constriction rates yet have a comparable molecular composition.

Cytokinesis nodes are present in *Δmid1* cells

As the type of strand that produces the contractile ring predicts its constriction rate, nascent and enduring strands may have distinct molecular organizations. We used high-speed SMLM in live cells to visualize the arrangement of cytokinesis proteins in the strands and contractile rings of *Δmid1* cells (Laplante et al., 2016a; Laplante et al., 2016b). We imaged live cells expressing endogenously tagged Cdc12p, Cdc15p, Rng2p, and Myo2p with mEos3.2 at either their carboxy or amino terminal in face or side views (Fig. 2 A; Bähler et al., 1998b; Zhang et al., 2012). We compiled a map of the coordinates of all localized single-molecule emissions for a selected number of camera frames, generated images for visualization purposes, and color-coded them for their time of emission during the acquisition (rainbow colormap) or density (heat colormap; Fig. 2 B; and Fig. S1, F and G). Quantitative measurements were performed on raw localization data using single-molecule analysis algorithms, not on the visualization images (Laplante et al., 2016b).

SMLM revealed the presence of nodes in all the cytokinesis structures in wild-type cells: bands, assembling contractile rings, and constricting contractile rings (Fig. 2, C and D; Laplante et al., 2016b). Consistent with simulations, we found that nodes align onto strands in wild-type cells during contractile ring assembly, suggesting that strands of nodes are a normal intermediate structure (Fig. 2, C and D; Vavylonis et al., 2008). These nodes are packed too closely together to be distinguished by confocal microscopy. Strands of nodes likely correspond to nodes bound to actin filaments or bundles of actin filaments as they are not observed in cells treated with latrunculin A (LatA), which depolymerizes the actin filaments (Fig. S1 B). Nodes in constricting contractile rings are densely packed but are clearly distinguished in images reconstructed using fewer camera frames (Fig. 2, D and E).

We observed nodes in both nascent and enduring strands and in constricting contractile rings of *Δmid1* cells (Fig. 2 E). Nodes in nascent strands organize into short connected strings, similar to the general morphology of nascent strands observed by confocal microscopy. Nodes in enduring strands align onto long strands that span the length of the cell (Fig. 2 E). Nodes in the contractile ring of *Δmid1* cells are densely packed as in wild-type cells. To differentiate between the types of nodes, we use the term "precursor nodes" (P-nodes) to refer to nodes found in the broad band and strands. We use the term "ring nodes" (R-nodes) to refer to nodes of the contractile ring.

We determined whether P-nodes align onto strands in *Δmid1* because they are bound to actin filaments. We treated wild-type and *Δmid1* cells with 5 µM LatA to depolymerize the actin filament network, quickly mounted them, and started time-lapse confocal imaging within 2–3 min of addition of the drug. P-nodes in strands disperse along the cell cortex within 10 min of drug addition (Fig. S1 C). We observed the same outcome with R-nodes in both wild-type and *Δmid1* cells. We obtained comparable results with 100 µM LatA except with faster node dispersal after the addition of the drug. Therefore, depolymerizing the actin network releases P-nodes and R-nodes from strands and contractile rings.

Myo2p heads adopt a distinct distribution in P-nodes of nascent and enduring strands

We determined whether P-nodes in nascent and enduring strands exhibit distinct molecular organizations that correlate with the different constriction rates of the contractile ring they produce. In wild-type cells, each cytokinesis protein adopts a signature molecular organization, defined by its radial density distribution, dimension, and number of localized single-molecule emissions in nodes (Laplante et al., 2016b). This general organization is maintained after the contractile ring is assembled (Laplante et al., 2016b). We determined the molecular organization of cytokinesis proteins in P-nodes in *Δmid1* and wild-type cells by measuring the radial density distribution and the dimension of their cytokinesis proteins. Cells expressing cytokinesis proteins endogenously tagged with mEos3.2 and expressing the *cdc25-22* mutations were arrested at the G2/M transition and released as a synchronous population to enrich populations for cells in cytokinesis.

Each cytokinesis protein occupies an area of distinct radius ranging from 34–50 nm within the P-nodes of the equatorial band of wild-type cells before SPB separation (Fig. 3 A; Laplante et al., 2016b). The formin Cdc12p-mEos3.2 distributes within the smallest area of 34 nm in radius followed by the tips of myosin-II tails Myo2p-mEos3.2, mEos3.2-Rng2p, mEos3.2-Cdc15p, Cdc15p-mEos3.2, and finally the heads of myosin-II mEos3.2-Myo2p occupying the largest area at 50 nm in radius. We imaged

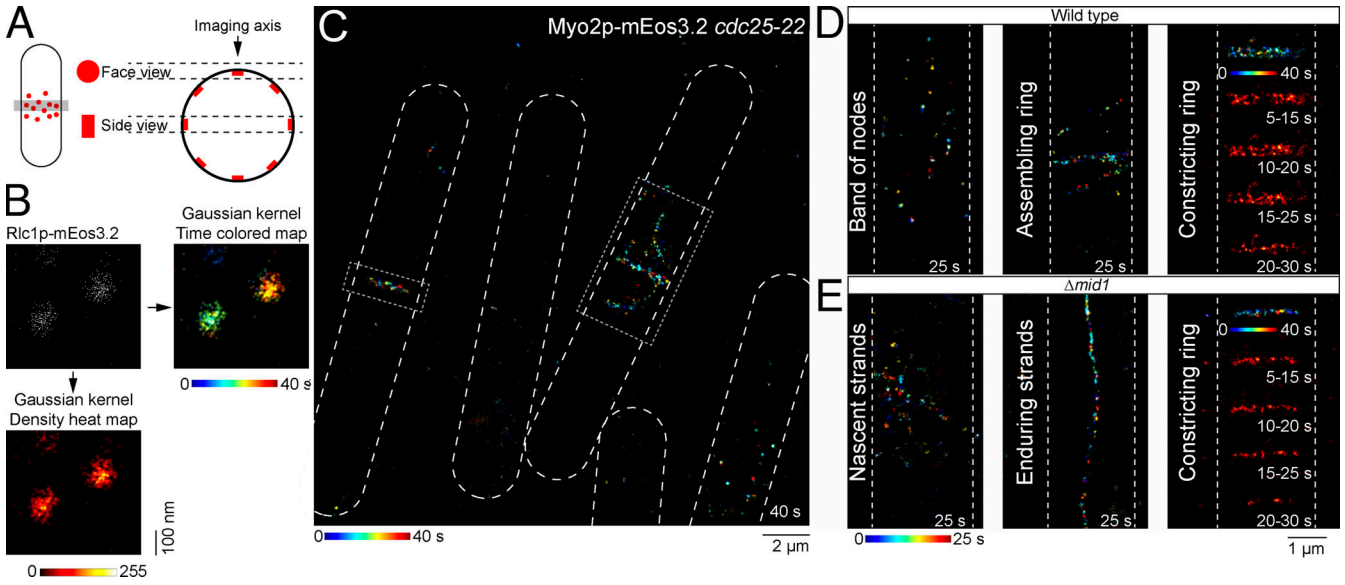

Figure 2. **Nodes are present in all cytokinesis structures of wild-type and *Δmid1* cells. (A)** Diagrams of a fission yeast cell viewed from the surface (left) and cross-section (right) showing face and side views. **(B)** Face views of P-nodes. Raw localizations (top left), visualization reconstruction images color-coded for density (bottom left) or time of detection (top right). **(C)** Reconstructed image of the face view of a field of cells using 40 s acquisition (8,000 camera frames). **(D and E)** Reconstructed images of wild-type (D) and *Δmid1* cells (E) expressing Myo2p-mEos3.2 or mEos3.2-Myo2p. Cropped images of contractile rings in wild-type and *Δmid1* cells are shown as both 40 s and sequential 10 s reconstructions to demonstrate the R-node density within these structures. Duration of acquired data used for the reconstructions at the bottom of each panel.

P-nodes in the equatorial band in side views by acquiring SMLM data across the middle of the cells (Figs. 2 A and S2 A). The molecular organization, size, and distribution of these proteins are comparable with those measured previously (Laplante et al., 2016b). We obtained the same inverted bouquet organization for Myo2p with the tip of Myo2p tails grouped close to the edge of the cell and their heads fanning out into the cytoplasm (Fig. S2 C).

The molecular organization of Cdc12p-mEos3.2, Myo2p-mEos3.2, mEos3.2-Rng2p, mEos3.2-Cdc15p, and Cdc15p-mEos3.2 within *Δmid1* strand P-nodes and wild-type band P-nodes are comparable (Fig. 3, A and C; and Fig. S2 D, F, and G). In contrast, the Myo2p heads group more tightly in the strand P-nodes in *Δmid1* cells. In the P-nodes of nascent strands, the Myo2p heads spread into a zone of 43 nm in radius, 7 nm smaller than P-nodes of wild-type cells (Fig. 3 C). In the P-nodes of enduring strands, the Myo2p heads spread into a zone of 36 nm in radius, 14 nm smaller than in the P-nodes of wild-type cells. These measurements suggest that the overall molecular organization of cytokinesis proteins within nodes is independent of the presence of Mid1p. Yet the spreading of the Myo2p heads is progressively tighter in P-nodes of wild-type bands, *Δmid1* nascent strands, and *Δmid1* enduring strands. We could not analyze the side view of strand P-nodes as their density and stacking within the thickness of the optical plane precludes the cropping and analysis of single nodes.

The difference between the distribution of the Myo2p heads in the P-nodes of different structures may be caused by the presence of actin filaments in *Δmid1* cells. We arrested wild-type and *Δmid1 cdc25-22* cells at the G2/M transition, added 100 µM LatA for the last 30 min at high temperature, and released them at room temperature before imaging. P-nodes appeared ∼50 min after shifting the cell cultures to room temperature in both genotypes, confirming that cytokinesis nodes assemble in the absence of actin filaments in wild-type or *Δmid1* cells. In wild-type cells, a band of P-nodes assembled at the equator but did not coalesce into a contractile ring in the absence of actin (Fig. 3 D; Wu et al., 2006). In contrast, P-nodes appeared randomly across the cortex in *Δmid1* cells as cortical complexes with no bias for the cell equator or other presumptive division plane. Type 2 interphase nodes labeled with Blt1p show a comparable distribution in *Δmid1* treated with LatA (Saha and Pollard, 2012a). Loss of Mid1p thus results in the absence of a zone of competence for the assembly of a band of P-nodes, possibly because type 1 interphase nodes are not confined to an equatorial band in the absence of Mid1p. In these cells, the Myo2p heads distribute in a relaxed zone of 49 nm radius, comparable with the size of the zone occupied by Myo2p heads in the band of P-nodes of wild-type cells and LatA-treated wild-type cells (Figs. 3 E; and S2, B and E). The presence of actin filaments in *Δmid1* cells thus influences the distribution of Myo2p heads in the P-nodes of nascent and enduring strands.

The numbers of localized emitters for each protein analyzed in all structures for both wild-type cells and *Δmid1* cells are comparable with stoichiometric ratios of one dimer of Cdc12p to two dimers of Cdc15p, Rng2p, and Myo2p (Fig. S2 H). The stochastic blinking of mEos3.2 combined with limiting out analyses to 1,000 camera frames are likely responsible for the high variability in the number of localizations per node.

We built molecular models of the face view of cytokinesis nodes constrained by our measurements of size and stoichiometries of four cytokinesis proteins labeled on six

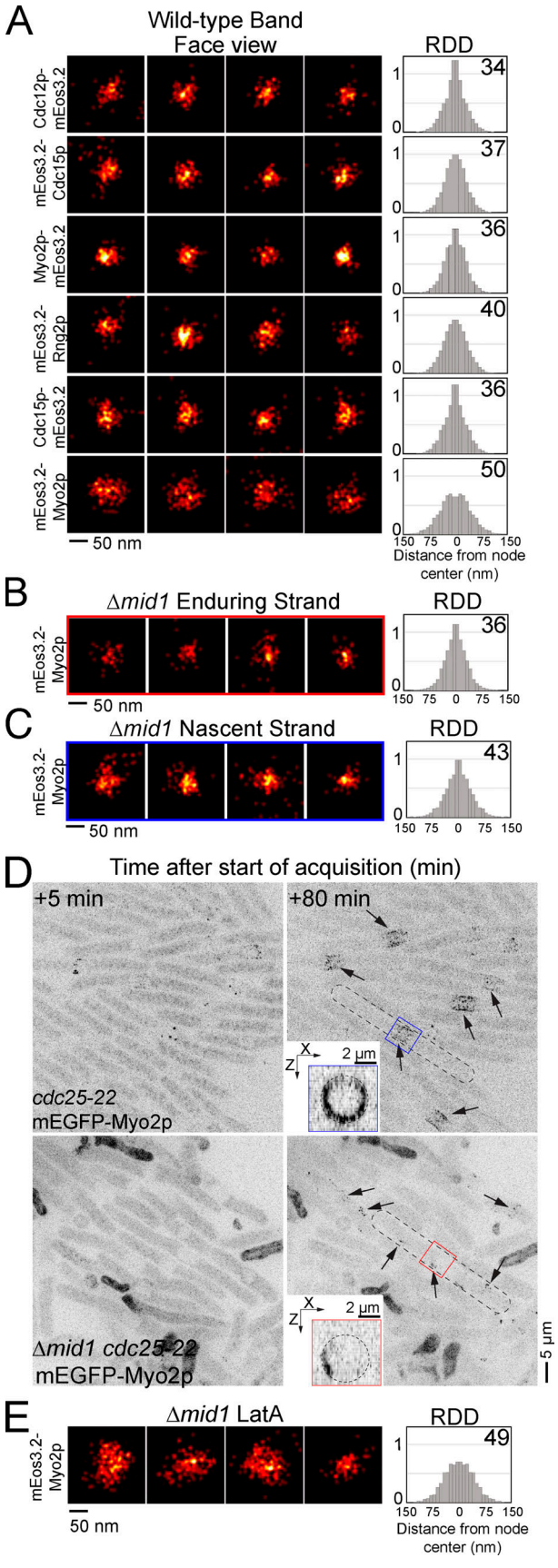

Figure 3. **Myo2 heads distribution differs in different types of P-nodes. (A)** SMLM images of P-nodes from equatorial bands of wild-type cells acquired in face view labeled with six different cytokinesis proteins fused to mEos3.2. Four examples shown to represent variability. Radial density distributions (RDDs) of localized single molecules for each node protein. Data mirrored at the origin. Numbers in the top right, node radii (nm). **(B and C)** SMLM images and RDD plots of face views of mEos3.2-Myo2p in the P-nodes of enduring and nascent strands of *Δmid1* cells. **(D)** Confocal micrographs of arrested and released cells treated with 100 µM LatA. Arrows point to P-nodes. Inset, orthogonal view of a band of P-nodes (top) or nascent strands (bottom) showing cortical localization. **(E)** SMLM images and RDD plot of face view P-nodes in LatA-treated *Δmid1* cells.

sites (Laplante et al., 2016b). Our results support three models of the cytokinesis node based on the distribution of the Myo2p heads (Fig. 4 C). Model I illustrates the broad distribution of Myo2p heads in the absence of actin filaments. Model II illustrates the narrow distribution of the Myo2p heads in the P-nodes of nascent strands of *Δmid1* cells. Model III illustrates the most compact distribution of Myo2p heads found in enduring strands of *Δmid1* cells.

Molecular organizations of R-nodes are comparable between wild-type and *Δmid1*

We measured protein distribution and node dimensions in the R-nodes of constricting contractile rings in wild-type and *Δmid1* cells using SMLM. We focused on constricting contractile rings that have completed between 20–50% of their constriction as the higher density of R-nodes in contractile rings that have constricted by more than 50% precludes the cropping and analysis of single nodes. The molecular organization of the cytokinesis proteins were comparable between R-nodes of wild-type and *Δmid1* cells except for Cdc12p (Fig. 4, A and B; and Fig. S2, F and G). In the contractile rings of both wild-type and *Δmid1* cells, the Myo2p heads distributed in a zone of 43 nm radius, agreeing with our molecular model II (Fig. 4 C). Cdc12p distributed in a smaller zone in the R-nodes of *Δmid1* cells. The rapid photobleaching of fluorescent probes by SMLM in live cells limits the acquisition to short durations, precluding the identification of the type of strand that generated the contractile ring. The resulting molecular organization thus represents the ensemble of contractile rings made from nascent and enduring strands.

The number of localized emitters for each tagged protein was not significantly different between R-nodes of wild-type and *Δmid1* cells (Fig. S2 I). We did not analyze the side view of R-nodes as their high density precludes cropping and analyzing single nodes.

P-nodes assemble directly onto actin in *Δmid1* cells

Our results so far suggest that actin filaments are present at the time of P-node assembly in *Δmid1* cells, resulting in the alignment of P-nodes onto strands. We visualized the actin filament network using confocal time-lapse microscopy in wild-type and *Δmid1* cells coexpressing the actin marker GFP-CHD and the node protein Rlc1p-tdTomato to determine the timing and location of the appearance of actin filaments in the cells (Chen et al., 2012). In wild-type cells, Rlc1p-tdTomato appears as a band of distinct P-nodes before actin is polymerized at the division plane (Fig. 5 A; Laporte et al., 2011; Saha and Pollard,

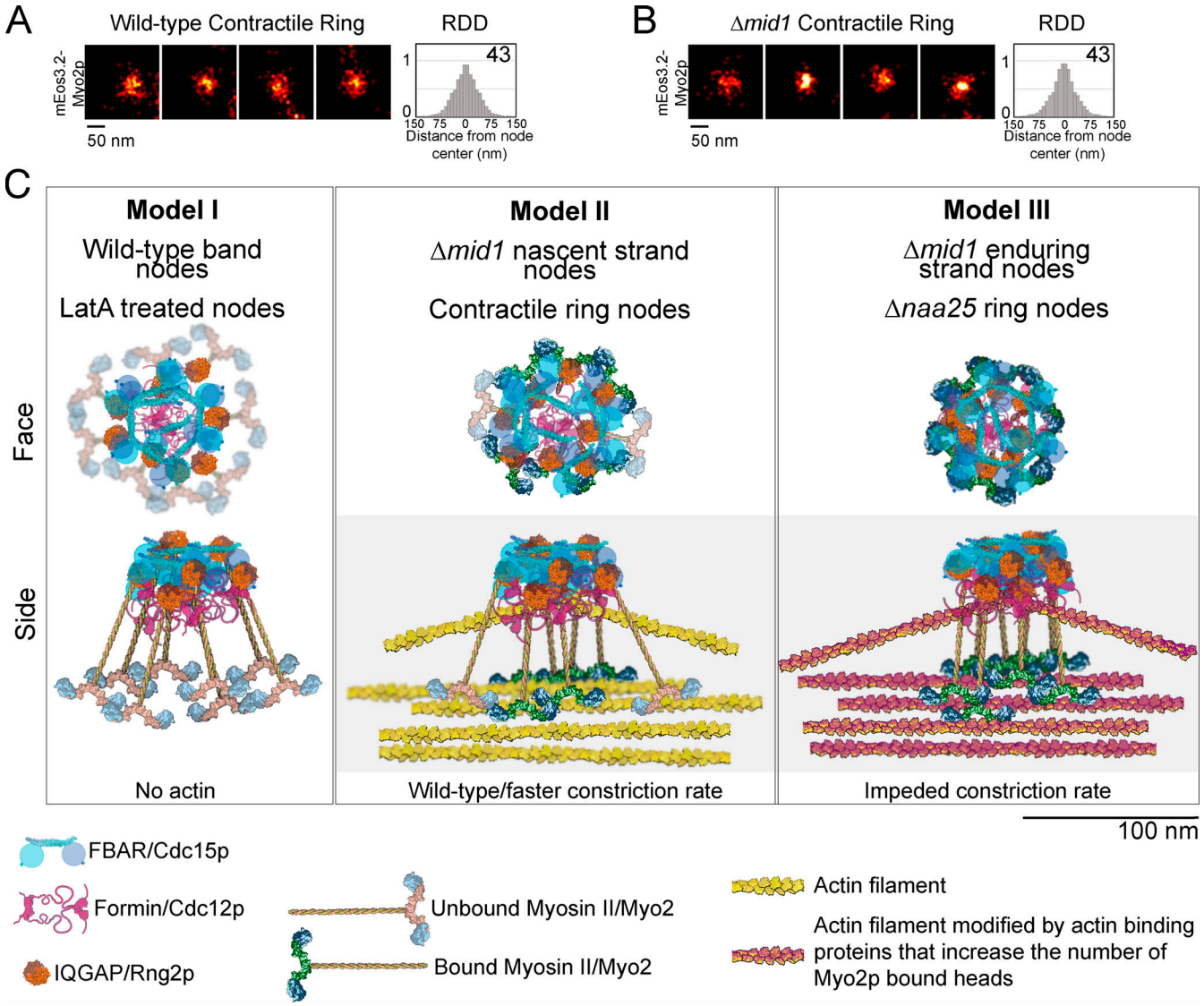

Figure 4. **The molecular organization of nodes conforms to three distinct models. (A and B)** Face-view SMLM images and RDD plots of R-nodes of wild-type (A) and *Δmid1* (B) cells. **(C)** Molecular models of the cytokinesis nodes in face (top) and side (Model I, bottom) views were built using the calculated node radii, radial density distributions, stoichiometries, and available protein structures. Side views of nodes in Models II and III are interpretations based on the measurements of nodes in face views and the side-view measurements in Model I. Actin filaments are colored differently to represent distinct populations of actin. Molecules are drawn to scale. RDD, radial density distribution. IQGAP, IQ motif containing GTPase-activating protein; F-BAR, Fes/CIP4 homology-Bin/amphiphysin/Rvs.

2012a; Wu et al., 2003; Wu et al., 2006). In contrast, cytoplasmic aggregates of actin filaments appear near the poles of *Δmid1* cells at +5 min (Fig. 5, A and C). These aggregates rapidly move to the presumptive division plane, where they connect with the cortex 10 min after SPB separation (Fig. 5, A and B).

We measured the timing of protein recruitment in *Δmid1* cells. In wild-type cells, cytokinesis proteins sequentially join the band of P-nodes at the division plane with Myo2 molecules and Rng2p at −10 min, Cdc15p at −2 min, and finally Cdc12p at 0 min after SPB separation (Fig. 5 C; Laporte et al., 2011; Wu et al., 2003; Wu et al., 2006). In *Δmid1* cells, the same proteins are first recruited to the protein aggregates at the poles of the cell at +5 min (Fig. 5, A–C). The aggregates travel to the presumptive division plane, where they connect with the plasma membrane and become nascent strands 10 min after SPB separation. We observed a similar timing of appearance of nascent strands (+7 min) in *mid1-366* cells. We reserve the term nodes for cortical protein complexes (Wu et al., 2006). Therefore, cytoplasmic aggregates with no obvious contact with the cortex are not called nodes. Our observations show that the recruitment of cytokinesis proteins into P-nodes is delayed with no obvious chronological hierarchy in the absence of Mid1p.

The appearance of actin aggregates near the poles of the cells suggests a local bias for actin polymerization near the poles. In wild-type cells, the actin polymerization factor formin For3p localizes at the poles of the cells during interphase (Martin and Chang, 2006) and relocates to the fully formed contractile ring at +12 min (n = 12 cells; Fig. S3 C). The transition from the cell tips

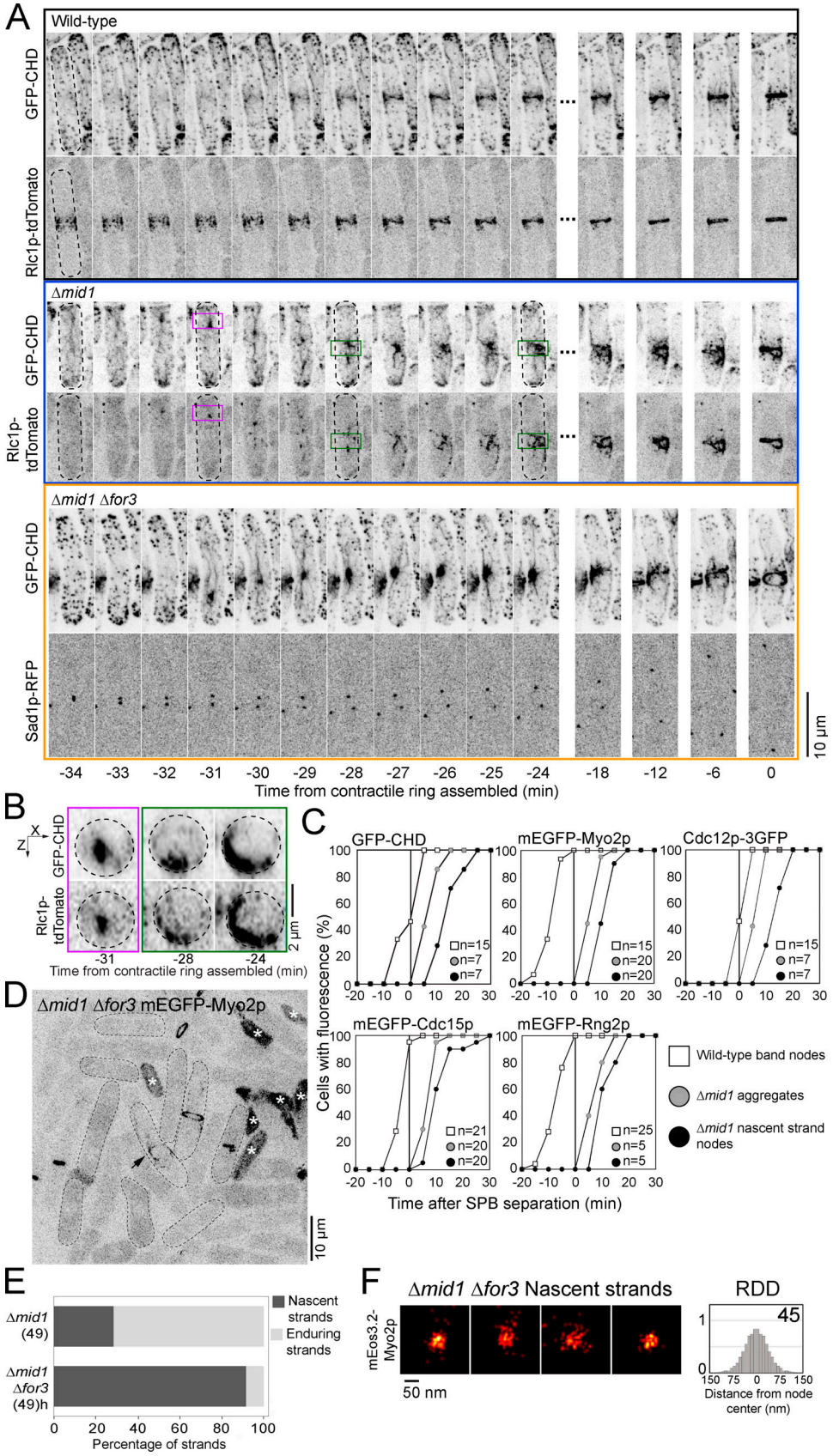

Figure 5. **P-nodes assemble directly onto actin in *Δmid1* cells. (A)** Time series of confocal micrographs of wild-type (top), *Δmid1* (middle), or *Δmid1 Δfor3* (bottom) cells. **(B)** Orthogonal views of boxed regions in A (*Δmid1* cell; seven optical planes). **(C)** Outcomes plot showing the accumulation of actin filaments and cytokinesis proteins in the P-nodes of the equatorial band in wild-type cells, the nascent strands of *Δmid1* cells, or the aggregates at the poles of *Δmid1* cells

over time. **(D)** Confocal micrograph of a field of cells. Arrow points to nascent strand. Asterisks mark dead cells. **(E)** Bar graph of the percentage of each type of strands in *Δmid1* and *Δmid1 Δfor3* cells. **(F)** Face views of SMLM images and RDD plot of P-nodes in *Δmid1 Δfor3* cells. Number of cells counted in brackets (C and E). RDD, radial density distribution.

to the contractile ring occurs over a short 2-min period. During constriction, For3p-3GFP localizes to both the contractile ring and the ingressing membrane overlapping with the growing septum. In *Δmid1* cells, For3p-3GFP relocates from the cell tips to the presumptive division plane as in wild-type cells and appears in nascent strands at +16 min (n = 10 cells), ∼10 min after P-nodes appear to the nascent strands and ∼7 min before the contractile ring is assembled. For3p-3GFP localizes to constricting contractile rings as in wild-type (Fig. S3 A), but no signal was observed along the ingressing plasma membrane, possibly due to the weak For3p-3GFP signal, making it hard to detect.

To test whether For3p polymerizes the actin filaments within the aggregates in *Δmid1* cells, we generated *Δmid1 Δfor3* double-mutant cells and visualized their actin network using the GFP-CHD actin marker. Under otherwise wild-type conditions, lack of For3p does not affect the assembly of the equatorial band of P-nodes or the timing of cytokinesis protein recruitment to P-nodes (Coffman et al., 2013). In *Δmid1 Δfor3* cells, actin filament aggregates appear near the poles and translocate to the presumptive division sites, indicating that For3p is dispensable for the polymerization of the actin aggregates in *Δmid1* cells. Cytokinesis proteins in *Δmid1 Δfor3* cells are recruited to nascent strands with similar timing as in *Δmid1* cells (Fig. S3 B).

Enduring strands were rarely observed in *Δmid1 Δfor3* cells, suggesting that For3p plays an important role in the formation or the maintenance of enduring strands (Fig. 5, D and E). The formation of nascent strands and their proportion in the cell population were not changed in *Δmid1 Δfor3* cells, suggesting that For3p is dispensable for nascent strands. The heads of Myo2p distribute in a radius of 45 nm in the nascent strands of *Δmid1 Δfor3* cells, comparable with the size of the Myo2p head distribution in the nascent strands of *Δmid1* cells (Fig. 5 F). The average constriction rate of contractile rings in *Δmid1 Δfor3* cells is 0.35 µm/min, similar to the fast population of constricting contractile rings made by nascent strands in *Δmid1* cells (Fig. 1, E and F). For3p-3GFP localizes to both nascent and enduring strands; therefore, the presence of For3p is not sufficient to explain its requirement for the enduring strands (Fig. S3 A).

The morphology of *Δmid1 Δfor3* cells was similar to that of wild-type cells, with fewer branched cells (1%, n = 67 *Δmid1 Δfor3* cells compared with 24%, n = 94 *Δmid1* cells). We also observed fewer multiseptated cells in the population, suggesting that removing For3p from *Δmid1* cells partially rescues the *Δmid1* cell morphology and cytokinesis phenotypes (Fig. 5 D).

Acetyltransferase function is required for tight distribution of Myo2p heads in P-nodes of enduring strands

The tight 36 nm radius distribution of Myo2p heads is only observed in the P-nodes of For3p-dependent enduring strands. Could formin For3p polymerize molecularly distinct actin filaments affecting the distribution of the Myo2p heads? In fission yeast, tropomyosin/Cdc8p exists in acetylated and unacetylated states, with a high ratio of acetylated to unacetylated in the cell and in the contractile ring (Coulton et al., 2010; Johnson et al., 2014; Skoumpla et al., 2007). Actin polymerized by For3p is decorated with unacetylated Cdc8p, whereas actin polymerized by Cdc12p is decorated with acetylated Cdc8p (Coulton et al., 2010). Therefore, the choice of formin may influence the acetylation state of Cdc8p, in turn affecting the molecular distribution of Myo2p heads and contractile ring constriction rate.

We tested whether the acetylation state of Cdc8p affects cytokinesis in cells that lack Naa25p, the NatB N-acetyltransferase complex regulatory subunit essential for the acetylation of Cdc8p (Coulton et al., 2010). We assume that actin filaments are decorated with unacetylated Cdc8p in *Δnaa25* cells. We acquired confocal time-lapse micrographs of *Δnaa25* cells expressing mEGFP-Myo2p as a marker of the contractile ring. About half of the *Δnaa25* cell population shows the presence of cytokinesis structures with a strong bias for cells with a band of P-nodes over cells with contractile rings, suggesting that P-node coalescence into a contractile ring is defective in *Δnaa25* cells (Fig. 6 A).

Time-lapse confocal microscopy images show that *Δnaa25* cells assemble a band of P-nodes at their equator 10 min before SPB separation, comparable with wild-type cells (Fig. 6 B). However, the P-nodes in the band disperse away from the equator starting at +30 min. As they disperse, the P-nodes align into multiple short strands. The strands can eventually make a ring that constricts slowly at a rate of 0.17 µm/min, comparable with the constriction rate of contractile rings made from enduring strands in *Δmid1* (Fig. 1, E and F). We measured no significant differences in the fluorescence intensity of mEGFP-Myo2p and Cdc12p-3GFP in constricting contractile rings in *Δnaa25* and wild-type cells, suggesting that the overall composition of these contractile rings is comparable (Fig. S3 D).

We determined whether the acetylation state of Cdc8p affects the distribution of Myo2p heads. We found that the Myo2p heads in R-nodes of *Δnaa25* cells distribute in a zone of 37 nm (Fig. 6 D). The Myo2p heads distribute in a zone of 51 nm in the band of P-nodes in *Δnaa25* cells, when actin is absent, similar to the distribution of Myo2p heads in the band of P-nodes in wild-type cells (Fig. 6 C). Therefore, the unacetylated tropomyosin results in the strong compaction of the Myo2p heads in *Δnaa25* R-nodes. Although contractile rings in *Δnaa25* cells assemble from the coalescence of a band of P-nodes, their constriction rate is comparable with that of contractile rings made from enduring strands in *Δmid1* cells. The common factor between these two different contexts is possibly the unacetylated state of Cdc8p.

Discussion

The molecular organization of the contractile ring governs its mechanics. Visualizing how molecules of the contractile ring are

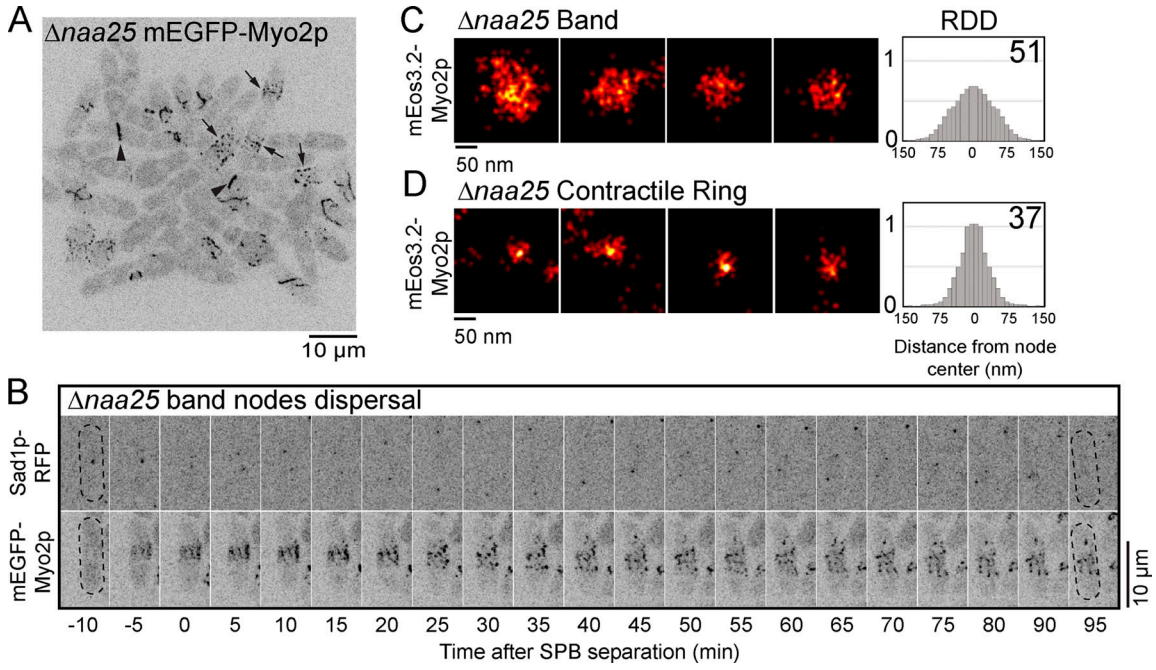

Figure 6. **For3p and actin composition modulate the strand type, Myo2p head distribution and constriction rate. (A)** Confocal micrographs of fields of *Δnaa25* cells. Arrows point to bands of P-nodes. Arrowheads point to contractile rings (left). **(B)** Time series of micrographs of *Δnaa25* cells. **(C and D)** Face views SMLM images and RDD plots of nodes in *Δnaa25* cells. RDD, radial density distribution. RFP, red fluorescent protein.

organized has been hindered by the limited availability of imaging techniques with suitable resolution. The emergence of super-resolution microscopy techniques has uncovered new paths to exploring the molecular organization of dense protein structures, such as the constricting contractile ring. Here, we use high-speed SMLM in live cells and show for the first time a predictive correlation between the molecular organization of cytokinesis proteins and the mechanics of constriction of the contractile ring.

Contractile rings in *Δmid1* cells assemble from the looping of either nascent or enduring strands, two distinct types of strands composed of actin filaments and cytokinesis proteins. Each type of strand produces contractile rings that constrict with distinct rates, suggesting that nascent and enduring strands have different molecular organizations. We found that the motor-heads of Myo2p spread differently in the P-nodes of each type of strand: 43 nm in the radius zone in P-nodes of the nascent strand and 36 nm in the radius zone in P-nodes of the enduring strand. Importantly, in the absence of actin filaments, such as in the P-nodes of the equatorial band in wild-type cells or when *Δmid1* cells are treated with LatA, Myo2p heads spread into a wide zone of ∼50 nm in radius.

The distribution of Myo2p heads in the absence of actin filaments is likely the combined outcome of the organization of the tips of the tails at the core of the node, the length of the Myo2p tails, and the motions of the unbound heads (Fig. 4 C). As the presence of actin filaments correlates with the more compact distribution of Myo2p motor-heads in nodes, the narrower distributions observed in *Δmid1* strands likely result from the binding of Myo2p motor-heads to actin filaments. Increasing the ratio of the number of bound to unbound heads per node would result in a smaller node radius and a more compact radial density distribution of the single molecules. This interpretation suggests that the ratio of bound to unbound Myo2p heads is increased in the P-nodes of enduring strands compared with nascent strands. Different modifications to the actin filaments in nascent and enduring strands may drive the binding of Myo2p motor-heads to actin filaments, thus altering the ratio of bound to unbound Myo2p heads per P-node. Different formins can confer different molecular identity to the actin filaments they polymerize via unknown mechanisms (Coulton et al., 2010). The formin For3p is essential for enduring strands, and actin filaments polymerized by For3p are decorated by unacetylated tropomyosin (Coulton et al., 2010). Actin filaments decorated by unacetylated tropomyosin thus possibly influence the Myo2p motor-head distribution by promoting more Myo2p motor-heads per node to bind actin filaments. Consistent with this interpretation, we reproduced the narrow ∼36-nm distribution of Myo2p motor-heads in the contractile rings of N-acetylase–deficient *Δnaa25* cells (Coulton et al., 2010). Further work will be necessary to determine how the acetylation of tropomyosin affects the binding of Myo2p and what other proteins remain unacetylated in *Δnaa25* cells.

Enduring strands assemble from nascent strands that fail to loop into contractile rings or from contractile ring that do not disassemble at the end of cytokinesis. The making of an enduring strand from one of those preexisting cytokinesis structures requires For3p. For3p may be required to polymerize actin for the enduring strand either de novo or in the form of actin cables that bundle with the nascent strand or disassembling contractile ring. Enduring strands are persistent structures, and cells that make a contractile ring from these strands are likely at

a different phase of the cell cycle than cells that make their contractile ring for a nascent strand from the coalescence of a band of P-nodes. As a result, the activity of important signaling pathways including the septation initiation network may be different across these cellular contexts. Specifically, the septation initiation network pathway regulates constriction, contractile ring integrity, and septation in wild-type cells and also the appearance of contractile rings in *Δmid1* cells (Huang et al., 2008; Schmidt et al., 1997; Wu et al., 2003). These different cellular contexts likely result in additional factors that impact contractile ring behavior like differential posttranslational modification of cytokinesis proteins that may alter the actin cytoskeleton.

Increasing the number of Myo2p motor-heads bound to actin filament causes a decrease in the constriction rate, but the mechanism is not intuitive based on the expected function of Myo2 as a tension generator. Consistent with our results, Stark et al. (2010) found that doubling the number of Myo2p in the cells decreases the rate of constriction. This outcome was attributed to myosin-II's role in actin filament turnover (Guha et al., 2005; Murthy and Wadsworth, 2005). More Myo2 bound to actin filaments may destabilize the actin filaments of the contractile ring, causing a decrease in its constriction rate. The molecular organization of Myo2p, with its heads interacting with the main bundle of actin filaments and its tails connecting to the plasma membrane via the rest of the node, suggests that Myo2p participates in anchoring the actin to the plasma membrane in addition to generating tension. Increasing the effective anchoring by connecting more Myo2p heads per node to the actin could hinder the constriction of the contractile ring. An optimal ratio of Myo2p heads bound to actin filaments may exist to achieve optimal constriction rate. A ratio of bound heads that exceeds the optimal range, such as in enduring strands, would be counterproductive and impedes constriction. Why nascent strands produce rings that constrict faster than wild-type rings is unclear, and further work will be necessary to identify other changes to the molecular organization of contractile rings made from nascent strands. Those changes may include but are not limited to increased contractile force by Myp2p and/or Myo51p, reduced drag forces, or increased rate of septum deposition.

The organization of the cytokinesis at the core of the nodes remains relatively constant across the different genotypes and across the P-nodes and R-nodes (Fig. S4 C). Some differences include the Cdc12p and carboxy terminus of Cdc15p. Tension on the node by pulling forces exerted from myosin-II on the actin filaments anchored at the core of the nodes could explain those differences in the spread of both proteins. However, factors other than tension must be involved to explain the difference in the dimensions of Cdc12p in the R-nodes of wild-type and *Δmid1* cells, which are likely under tension yet distribute in a smaller radius.

Nodes are not always unambiguously resolved by SMLM (McDonald et al., 2017; Swulius et al., 2018). In their work, McDonald et al. (2017) used SMLM in fixed cells to measure the distribution of many cytokinesis proteins in side views of contractile rings before the onset of constriction. Four known node proteins were imaged in face view, and the resulting localizations were convolved with a blurring Gaussian to build images for visualization. The uniformity of the signal was measured by the fluorescence intensity profile of a line drawn along the length of the contractile ring using the reconstructed images. The signal from these four node proteins was then determined to be homogenous, supporting the absence of nodes in the contractile ring. A combination of the laser power used during acquisition, image processing, and the use of the convolved reconstructed images for quantitative data analysis can explain the different appearance between their data and ours (Fig. S1, E–G). Fixation of the cells may also affect the photophysical properties of the photoconvertible molecules. Even with these differences, it is likely that R-nodes are present in the data shown by McDonald et al. (2017) based on the irregular appearance of their protein distribution in face view, and therefore we believe that although our interpretations are different, our data are not contradictory. Electron cryotomography showed the organization of actin filaments within the contractile ring (Swulius et al., 2018). Although nodes could not be resolved with this technique, an ∼60-nm gap between the actin filaments and the plasma membrane is consistent with the size of the core of cytokinesis nodes.

Contrary to previous interpretations of confocal microscopy data, Mid1p is dispensable for four cytokinesis proteins to assemble into P-nodes (Huang et al., 2008; Motegi et al., 2004; Wu et al., 2006). In *Δmid1* cells, P-nodes form in the presence of actin filaments, and binding of the Myo2p heads with the actin filaments likely causes the immediate alignment of P-nodes into strands, making it hard or impossible to resolve these P-nodes by confocal microscopy. The presence of interphase nodes and the detection of Cdc12p in P-nodes during cytokinesis in *Δmid1* cells hinted that P-nodes were present in the absence of Mid1p (Saha and Pollard, 2012a). Given the extensive network of interactions between node proteins, it is reasonable that cytokinesis proteins can form P-nodes in the absence of Mid1p (Carnahan and Gould, 2003; Celton-Morizur et al., 2004; Hachet and Simanis, 2008; Huang et al., 2008; Laporte et al., 2011; Paoletti and Chang, 2000; Roberts-Galbraith et al., 2009; Saha and Pollard, 2012a; Saha and Pollard, 2012b; Willet et al., 2015). In light of these new data, more investigation will be necessary to determine the mechanism of P-node assembly.

Deleting For3p from *Δmid1* cells partially rescues the branched morphology of *Δmid1* cells (Fig. 5 D). For3p polymerizes the actin cables that are important for the transport of cell polarity proteins necessary for tip growth (Feierbach and Chang, 2001; Martin and Chang, 2006). For3p localizes to cell tips by the function of the polarity protein Tea1p (Feierbach et al., 2004). Tea1p localizes to ectopic cortical sites in *Δmid1* cells and may contribute to their branched morphology by promoting the growth of ectopic cell tips by recruiting For3p (Saha and Pollard, 2012a). Deleting For3p may thus prevent ectopic tip growth due to the lack of actin cables.

Our data establish the nodes as basic units of cytokinesis. Our combined findings propose a new perspective on the organization of cytokinesis proteins within the contractile ring and how this molecular organization influences the mechanics constriction.

Materials and methods

Strains, growing conditions, and genetic and cellular methods

Table S1 lists the *Schizosaccharomyces pombe* strains described in this study. The strains were created using PCR-based gene targeting to integrate the constructs into the locus of choice and confirmed by PCR and fluorescence microscopy (Bähler et al., 1998b). Either *pFA6a-mEos3.2* or *(mEGFP)-kanMX6* or *pFA6a-kanMX6-P(gene of interest)-mEGFP* were used depending on whether C-terminal or N-terminal tagging of the gene was desired. Primers with 80 bp of homologous sequence flanking the integration site (obtained at www.bahlerlab.info/resources/) and two repeats of GGAGGT to create a 4xGly linker were used to amplify the vector of choice. With the exception of the GFP-CHD construct, all tagged genes were under the control of their endogenous promoter. Cells were grown in an exponential phase for 36–48 h before imaging. Cells expressing a construct under the *Pnmt41* promoter were shifted to EMM5S 15–18 h before imaging to allow expression of the construct. Both *Δmid1::natMX6* and *Δmid1::ura4+* genetic backgrounds were used in this study, as the duration of cytokinesis from SPB separation to contractile ring disassembly between *Δmid1::natMX6* cells ($n = 8$) and *Δmid1::ura4*$^+$ ($n = 7$) was not significantly different (Student's t test; $P = 0.4042$).

To synchronize the population of cells, we used the temperature-sensitive *cdc25-22* mutation to arrest cells at the G2/M transition at the restrictive temperature of 34°C for 4 h. We then released cells into mitosis at the permissive temperature of 22°C as a synchronized population. We did not use 36°C because both wild-type and *Δmid1* cells grown at that temperature exhibit high fluorescent cytoplasmic background noise interfering with SMLM imaging at that temperature.

Δmid1 cells can accumulate suppressor mutations overtime (Coffman et al., 2009; Lee and Wu, 2012; Tao et al., 2014). To avoid complications from different genetic backgrounds, all *Δmid1* cells used in this study were carefully compared to ensure that all phenotypes measured were the identical across all deletion strains. In addition, we freshly thawed yeast cultures from the −80°C stocks, grew them on YE5S plates for 2–3 d at 25°C, and then used them to prepare liquid cultures that were grown for 36 h before imaging. Plates and liquid cultures were discarded and replaced with fresh cultures on a weekly basis to prevent the accumulation of suppressor mutations. We grew *mid1-366* cells at the restrictive temperature of 35.5°C for 2.5 h before immediately imaging at room temperature.

Treatment with LatA to depolymerize the actin cytoskeleton was performed with either of the following two methods. To completely depolymerize the actin cytoskeleton, cells were treated with 100 µM LatA for 30 min before imaging. LatA was left in the medium before imaging as described in the Results section. For imaging while actin was being depolymerized, either 5 µM or 100 µM LatA was added to cells. The cells were mounted as described below and immediately imaged. We found comparable results with or without LatA added to the gelatin pad.

Spinning-disk confocal microscopy and data analysis

Cells were grown in exponential phase at 25°C in YE5S-rich liquid medium in 50-ml baffled flasks in a shaking incubator in the dark. Fluorescence images of live cells were acquired with a Nikon Eclipse Ti microscope equipped with a 100×/NA 1.49 HP Apo TIRF objective (Nikon), a CSU-X1 (Yokogawa) confocal spinning-disk system, 405/488/561/647-nm solid-state lasers, and an electron-multiplying cooled charge-coupled device camera (EMCCD IXon 897; Andor Technology). The Nikon Element software was used for acquisition. Cells were concentrated 10- to 20-fold by centrifugation at 2,400 *g* for 30 s and then resuspended in EMM5S. 5 µl of cells was mounted on a thin gelatin pad consisting of 10 µl 25% gelatin (G-2500; Sigma-Aldrich) in EMM5S, sealed under a no. 1.5 coverslip with 1:1:1 vaseline/lanolin/parafin, and observed at room temperature or 22°C.

ImageJ (Schneider et al., 2012) and/or Nikon Element were used to create maximum-intensity projections of images, montages, and other image analyses. Images in the figures are maximum-intensity projections of z-sections spaced at 0.36 µm. Images were systematically contrasted to provide the best visualization, and images within the same figure panel were contrasted using the same settings. Confocal fluorescence micrographs in the figures are shown as inverted grayscale look-up table (LUT). Ring constriction rate was measured using kymographs of maximum projection images (19 z-confocal planes taken for 6.48 µm) of time-lapse datasets taken at 1-min time intervals. The kymographs were thresholded, and the circumference was calculated automatically for each time point. These values were plotted in Microsoft Excel, and the constriction rate was calculated using a linear regression. Student's t tests were used to determine whether constriction rates differed significantly between planned comparisons of strains.

To count proteins in contractile rings, we created sum projection images of fields of cells from stacks of 19 optical images separated by 0.36 µm (Wu et al., 2008; Wu and Pollard, 2005). The images were corrected for the camera noise and uneven illumination, and then the fluorescence intensity of contractile rings was measured. These fluorescence intensity measurements were compared against a standard curve of proteins tagged endogenously with mEGFP to determine the number of molecules per contractile ring (Fig. 1 G; Wu et al., 2008; Wu and Pollard, 2005). Two-sample Kolmogorov–Smirnov (KS) tests were used to determine whether the distribution of polypeptides in the constricting contractile ring differed between wild-type and *Δmid1* cells. The null hypothesis is that the samples are drawn from the same distribution of polypeptides. The cumulative distribution functions (CDFs) for polypeptide number were calculated for each of the markers and genetic backgrounds, and the maximum difference between pairs of CDFs was calculated and compared with the KS test critical value at a significance level of $P < 0.05$. If the maximum difference between the CDFs was greater than the critical value, the null hypothesis was rejected.

Coefficients of variation between the distributions were calculated for all rings <9.5 µm in circumference. Rings larger than this were excluded from the calculate to remove assembling rings.

Super-resolution data acquisition and display

Super-resolution imaging was performed with a Nikon STORM system operating in 2D mode, calibrated for single-molecule acquisition in live cells. We used epi illumination to photoconvert and excite the fluorophores. We imaged single molecules with an sCMOS camera (ORCA-Flash4.0; Hamamatsu) operating at 200 frames per second using Nikon Elements software. Power for both 405- and 561-nm lasers was optimized for distinct minimally overlapping single-molecule emissions. We tested combinations of 405-nm and 561-nm laser powers first visually for single-molecule emission and then quantitatively for localized single molecules (Fig. S1, D and E). The average laser power density of the 561-nm laser used to excite the photoconverted mEos3.2 for imaging was ∼0.3 kW/cm^2, illuminating a ∼5,500 µm^2 area. To maintain a density of photoconverted mEos3.2 at an appropriate level for single-molecule localizations, the power of the 405-nm laser used for photoconversion was increased manually every 5 s during data acquisition. The total power of the 405-nm laser ranged from 0 to 32 µW.

Acquired data were processed to localize single molecules as previously described (Laplante et al., 2016a; Laplante et al., 2016b). Acquired frames were analyzed using a custom sCMOS-specific localization algorithm based on a maximum likelihood estimator as described previously (Huang et al., 2013; Laplante et al., 2016a; Laplante et al., 2016b). A log-likelihood ratio was used as the rejection algorithm to filter out overlapping emitters, nonconverging fits, out-of-focus single molecules, and artifacts caused by rapid movements during one camera exposure time (Huang et al., 2013; Huang et al., 2011). The accepted estimates were reconstructed in a 2D histogram image of 5-nm pixels, where the integer value in each pixel represented the number of localization estimates within that pixel. Images for visualization purposes were generated with each localization convolved with a 2D Gaussian kernel (σ = 7.5 nm; Fig. S1 F). Images were reconstructed from all or a subset of acquired frames and color-coded for either the temporal information (jet LUT map) or for localization density (heat LUT map). Our localization algorithm eliminated out-of-focus emissions, providing an effective depth of field of ∼400 nm (Laplante et al., 2016b).

Node identification and measurements

Cytokinetic P-nodes and R-nodes can be viewed from either the plane of the plasma membrane (face view) or the side by focusing on the central section of the cell (side view). Clusters of localized emitters associated with cytokinesis structures were manually selected from the reconstructed SMLM images. Face views and side views for were analyzed for P-nodes in equatorial bands. Only face views were analyzed for R-nodes and P-nodes in strands. For comparison purposes, all nodes were cropped from images reconstructed from 1,000 frames (5 s) to minimize blurring due to crowding and movement and allow for the selection of individual P-nodes and R-nodes.

The edge of the cell was identified by increasing the brightness of SMLM images to enhance the cytoplasmic background. The edge of the cell was located where the cytoplasmic background drops off at the interface with the space outside the cells (Laplante et al., 2016b).

We analyzed R-nodes from contractile rings that had constricted by 20–50%. R-nodes were difficult to segment if the contractile ring were constricted by >50% due to the density and movement of the R-nodes. All nodes were cropped using a 309 × 309–nm box in MATLAB.

We used the spatial and temporal information provided by each localized mEos3.2 emitter to measure the dimensions and stoichiometry of proteins within P-nodes and R-nodes. By treating each localized emitter as an independent measurement and using the large number of localizations, the radial density distribution approach becomes more robust than typical line profile measurements of fluorescence intensity.

Individual P-nodes and R-nodes were cropped, and the radial density distribution of their single-molecule emitters was plotted as previously described (Laplante et al., 2016b). We reconstructed position estimates of the emitters in 2D histogram images from face views of isolated P-nodes and R-nodes obtained from the cropping step with pixel size of 2 nm to avoid pixelation errors in the subsequent measurement analysis. These images were then fit with a rotationally symmetric 2D Gaussian model with amplitude and σ and center position in x and y as the fitting parameters. The radial symmetry centers of each node (Parthasarathy, 2012) were determined and used as the initial guesses for the x, y center in the fitting. Maximum likelihood estimator–based regression was performed assuming a Poisson noise model of the 2D histogram image using the Nelder–Mead simplex algorithm implemented in the MATLAB "fminsearch" function. Fitting estimates were filtered by their likelihood values thereafter. Fitting results that did not converge properly and resulted in center positions outside the image boundary or extremely large or small σ values were also discarded from the final results. This step eliminates instances where two objects were included in the same 309 × 309–nm selection box and includes only selections containing a single cluster. For each R-node accepted through the filtering process, the distances of individual localizations from the estimated node center were calculated. All distances measured from a specific node type and view were plotted into histograms and then subsequently normalized by their radius to give a radial density distribution. The number of localizations per identified node was recorded as well.

We used a two-sample KS test to compare the distribution of localizations in each pair of node proteins (Fig. S4, A and B). The null hypothesis is that the samples are drawn from the same distribution of localized emitters. The CDFs of the squared radial distance were calculated for each of the samples (Fig. S4, A and B), and the maximum difference between pairs of CDFs was calculated and compared with the KS test critical value at a significance level of $P < 0.05$ or $P < 0.005$. If the maximum difference between the CDFs was greater than the critical value, the null hypothesis was rejected. The results of the KS test comparisons and sample size of the super-resolution datasets can be found in Fig. S4, A and B.

The radius of each node marker was calculated using the CDF plots and was defined as the distance from the center of the node that contained 75% of the localized emitters (Fig. S2 A).

Quantification of localized emitters

For each marker and genetic background, we measured the total number of localized emitters per P-node and R-node. The number of localized emitters per node is influenced by many factors, including the total number of frames used for the reconstruction, the photophysics of the fluorescent proteins, the number of tagged proteins per node, and the autofluorescent background.

We used an ANOVA with Tukey's Honestly Significant Difference (HSD) test to compare the number of localizations per node between genotypes at a significance level $P < 0.05$ (Fig. S2, H and I). Box and whisker plots were generated using JMP Pro 14. The lower whisker represents 1st quartile − 1.5*(interquartile range). The upper whisker represents 3rd quartile + 1.5*(interquartile range).

Online supplemental material

Fig. S1 shows that P-nodes assemble in the absence of actin filaments. Fig. S2 shows molecular organization of node proteins. Fig. S3 shows localization and timing of For3p recruitment. Fig. S4 shows comparison of protein organization of cytokinesis proteins in the node. Table S1 lists the *S. pombe* strains described in this study.

Acknowledgments

We thank Nicolas Buchler, Samantha E.R. Dundon, Mary W. Elting, Fang Huang, Mohamed Moshtohry, and Thomas D. Pollard for valuable input. We thank Mohan Balasubramanian (The University of Warwick, Coventry, UK), Thomas D. Pollard (Yale University, New Haven, CT), and Juan C. Ribas (Universidad de Salamanca, Salamanca, Spain) for yeast strains.

This research was supported by National Institutes of Health research grant 5R01GM134254 to C. Laplante.

The authors declare no competing financial interests.

Author contributions: C. Laplante: conceptualization; data curation; funding acquisition; methodology; project administration; supervision; and writing, review, and editing. K. Bellingham-Johnstun: data curation; methodology; formal analysis; and writing, review, and editing. E.C. Anders: initial data curation. J. Ravi: software development. C Bruinsma: formal data analysis.

Submitted: 7 August 2020
Revised: 23 November 2020
Accepted: 22 December 2020

References

Akamatsu, M., J. Berro, K.M. Pu, I.R. Tebbs, and T.D. Pollard. 2014. Cytokinetic nodes in fission yeast arise from two distinct types of nodes that merge during interphase. *J. Cell Biol.* 204:977–988. https://doi.org/10.1083/jcb.201307174

Bähler, J., A.B. Steever, S. Wheatley, Y. Wang, J.R. Pringle, K.L. Gould, and D. McCollum. 1998a. Role of polo kinase and Mid1p in determining the site of cell division in fission yeast. *J. Cell Biol.* 143:1603–1616. https://doi.org/10.1083/jcb.143.6.1603

Bähler, J., J.Q. Wu, M.S. Longtine, N.G. Shah, A. McKenzie III, A.B. Steever, A. Wach, P. Philippsen, and J.R. Pringle. 1998b. Heterologous modules for efficient and versatile PCR-based gene targeting in Schizosaccharomyces pombe. *Yeast.* 14:943–951. https://doi.org/10.1002/(SICI)1097-0061(199807)14:10<943::AID-YEA292>3.0.CO;2-Y

Carnahan, R.H., and K.L. Gould. 2003. The PCH family protein, Cdc15p, recruits two F-actin nucleation pathways to coordinate cytokinetic actin ring formation in Schizosaccharomyces pombe. *J. Cell Biol.* 162:851–862. https://doi.org/10.1083/jcb.200305012

Celton-Morizur, S., N. Bordes, V. Fraisier, P.T. Tran, and A. Paoletti. 2004. C-terminal anchoring of mid1p to membranes stabilizes cytokinetic ring position in early mitosis in fission yeast. *Mol. Cell. Biol.* 24:10621–10635. https://doi.org/10.1128/MCB.24.24.10621-10635.2004

Chatterjee, M., and T.D. Pollard. 2019. The Functionally Important N-Terminal Half of Fission Yeast Mid1p Anillin Is Intrinsically Disordered and Undergoes Phase Separation. *Biochemistry.* 58:3031–3041. https://doi.org/10.1021/acs.biochem.9b00217

Chen, Q., S. Nag, and T.D. Pollard. 2012. Formins filter modified actin subunits during processive elongation. *J. Struct. Biol.* 177:32–39. https://doi.org/10.1016/j.jsb.2011.10.005

Coffman, V.C., A.H. Nile, I.J. Lee, H. Liu, and J.Q. Wu. 2009. Roles of formin nodes and myosin motor activity in Mid1p-dependent contractile-ring assembly during fission yeast cytokinesis. *Mol. Biol. Cell.* 20:5195–5210. https://doi.org/10.1091/mbc.e09-05-0428

Coffman, V.C., J.A. Sees, D.R. Kovar, and J.Q. Wu. 2013. The formins Cdc12 and For3 cooperate during contractile ring assembly in cytokinesis. *J. Cell Biol.* 203:101–114. https://doi.org/10.1083/jcb.201305022

Coulton, A.T., D.A. East, A. Galinska-Rakoczy, W. Lehman, and D.P. Mulvihill. 2010. The recruitment of acetylated and unacetylated tropomyosin to distinct actin polymers permits the discrete regulation of specific myosins in fission yeast. *J. Cell Sci.* 123:3235–3243. https://doi.org/10.1242/jcs.069971

Deng, L., and J.B. Moseley. 2013. Compartmentalized nodes control mitotic entry signaling in fission yeast. *Mol. Biol. Cell.* 24:1872–1881. https://doi.org/10.1091/mbc.e13-02-0104

Feierbach, B., and F. Chang. 2001. Roles of the fission yeast formin for3p in cell polarity, actin cable formation and symmetric cell division. *Curr. Biol.* 11:1656–1665. https://doi.org/10.1016/S0960-9822(01)00525-5

Feierbach, B., F. Verde, and F. Chang. 2004. Regulation of a formin complex by the microtubule plus end protein tea1p. *J. Cell Biol.* 165:697–707. https://doi.org/10.1083/jcb.200403090

Guha, M., M. Zhou, and Y.L. Wang. 2005. Cortical actin turnover during cytokinesis requires myosin II. *Curr. Biol.* 15:732–736. https://doi.org/10.1016/j.cub.2005.03.042

Guzman-Vendrell, M., S. Baldissard, M. Almonacid, A. Mayeux, A. Paoletti, and J.B. Moseley. 2013. Blt1 and Mid1 provide overlapping membrane anchors to position the division plane in fission yeast. *Mol. Cell. Biol.* 33:418–428. https://doi.org/10.1128/MCB.01286-12

Hachet, O., and V. Simanis. 2008. Mid1p/anillin and the septation initiation network orchestrate contractile ring assembly for cytokinesis. *Genes Dev.* 22:3205–3216. https://doi.org/10.1101/gad.1697208

Huang, Y., H. Yan, and M.K. Balasubramanian. 2008. Assembly of normal actomyosin rings in the absence of Mid1p and cortical nodes in fission yeast. *J. Cell Biol.* 183:979–988. https://doi.org/10.1083/jcb.200806151

Huang, F., S.L. Schwartz, J.M. Byars, and K.A. Lidke. 2011. Simultaneous multiple-emitter fitting for single molecule super-resolution imaging. *Biomed. Opt. Express.* 2:1377–1393. https://doi.org/10.1364/BOE.2.001377

Huang, F., T.M. Hartwich, F.E. Rivera-Molina, Y. Lin, W.C. Duim, J.J. Long, P.D. Uchil, J.R. Myers, M.A. Baird, W. Mothes, et al. 2013. Video-rate nanoscopy using sCMOS camera-specific single-molecule localization algorithms. *Nat. Methods.* 10:653–658. https://doi.org/10.1038/nmeth.2488

Johnson, M., D.A. East, and D.P. Mulvihill. 2014. Formins determine the functional properties of actin filaments in yeast. *Curr. Biol.* 24:1525–1530. https://doi.org/10.1016/j.cub.2014.05.034

Laplante, C., J. Berro, E. Karatekin, A. Hernandez-Leyva, R. Lee, and T.D. Pollard. 2015. Three myosins contribute uniquely to the assembly and constriction of the fission yeast cytokinetic contractile ring. *Curr. Biol.* 25:1955–1965. https://doi.org/10.1016/j.cub.2015.06.018

Laplante, C., F. Huang, J. Bewersdorf, and T.D. Pollard. 2016a. High-Speed Super-Resolution Imaging of Live Fission Yeast Cells. *Methods Mol. Biol.* 1369:45–57. https://doi.org/10.1007/978-1-4939-3145-3_4

Laplante, C., F. Huang, I.R. Tebbs, J. Bewersdorf, and T.D. Pollard. 2016b. Molecular organization of cytokinesis nodes and contractile rings by super-resolution fluorescence microscopy of live fission yeast. *Proc. Natl. Acad. Sci. USA.* 113:E5876–E5885. https://doi.org/10.1073/pnas.1608252113

Laporte, D., V.C. Coffman, I.J. Lee, and J.Q. Wu. 2011. Assembly and architecture of precursor nodes during fission yeast cytokinesis. *J. Cell Biol.* 192:1005–1021. https://doi.org/10.1083/jcb.201008171

Lee, I.J., and J.Q. Wu. 2012. Characterization of Mid1 domains for targeting and scaffolding in fission yeast cytokinesis. *J. Cell Sci.* 125:2973–2985. https://doi.org/10.1242/jcs.102574

Martin, S.G., and F. Chang. 2006. Dynamics of the formin for3p in actin cable assembly. *Curr. Biol.* 16:1161–1170. https://doi.org/10.1016/j.cub.2006.04.040

McDonald, N.A., A.L. Lind, S.E. Smith, R. Li, and K.L. Gould. 2017. Nanoscale architecture of the *Schizosaccharomyces pombe* contractile ring. *eLife.* 6: e28865. https://doi.org/10.7554/eLife.28865

Moseley, J.B., A. Mayeux, A. Paoletti, and P. Nurse. 2009. A spatial gradient coordinates cell size and mitotic entry in fission yeast. *Nature.* 459: 857–860. https://doi.org/10.1038/nature08074

Motegi, F., M. Mishra, M.K. Balasubramanian, and I. Mabuchi. 2004. Myosin-II reorganization during mitosis is controlled temporally by its dephosphorylation and spatially by Mid1 in fission yeast. *J. Cell Biol.* 165: 685–695. https://doi.org/10.1083/jcb.200402097

Murthy, K., and P. Wadsworth. 2005. Myosin-II-dependent localization and dynamics of F-actin during cytokinesis. *Curr. Biol.* 15:724–731. https://doi.org/10.1016/j.cub.2005.02.055

Paoletti, A., and F. Chang. 2000. Analysis of mid1p, a protein required for placement of the cell division site, reveals a link between the nucleus and the cell surface in fission yeast. *Mol. Biol. Cell.* 11:2757–2773. https://doi.org/10.1091/mbc.11.8.2757

Parthasarathy, R. 2012. Rapid, accurate particle tracking by calculation of radial symmetry centers. *Nat. Methods.* 9:724–726. https://doi.org/10.1038/nmeth.2071

Piekny, A.J., and A.S. Maddox. 2010. The myriad roles of Anillin during cytokinesis. *Semin. Cell Dev. Biol.* 21:881–891. https://doi.org/10.1016/j.semcdb.2010.08.002

Pollard, T.D. 2017. Nine unanswered questions about cytokinesis. *J. Cell Biol.* 216:3007–3016. https://doi.org/10.1083/jcb.201612068

Roberts-Galbraith, R.H., J.S. Chen, J. Wang, and K.L. Gould. 2009. The SH3 domains of two PCH family members cooperate in assembly of the Schizosaccharomyces pombe contractile ring. *J. Cell Biol.* 184:113–127. https://doi.org/10.1083/jcb.200806044

Saha, S., and T.D. Pollard. 2012a. Anillin-related protein Mid1p coordinates the assembly of the cytokinetic contractile ring in fission yeast. *Mol. Biol. Cell.* 23:3982–3992. https://doi.org/10.1091/mbc.e12-07-0535

Saha, S., and T.D. Pollard. 2012b. Characterization of structural and functional domains of the anillin-related protein Mid1p that contribute to cytokinesis in fission yeast. *Mol. Biol. Cell.* 23:3993–4007. https://doi.org/10.1091/mbc.e12-07-0536

Schmidt, S., M. Sohrmann, K. Hofmann, A. Woollard, and V. Simanis. 1997. The Spg1p GTPase is an essential, dosage-dependent inducer of septum formation in Schizosaccharomyces pombe. *Genes Dev.* 11:1519–1534. https://doi.org/10.1101/gad.11.12.1519

Schneider, C.A., W.S. Rasband, and K.W. Eliceiri. 2012. NIH Image to ImageJ: 25 years of image analysis. *Nat. Methods.* 9:671–675. https://doi.org/10.1038/nmeth.2089

Skoumpla, K., A.T. Coulton, W. Lehman, M.A. Geeves, and D.P. Mulvihill. 2007. Acetylation regulates tropomyosin function in the fission yeast Schizosaccharomyces pombe. *J. Cell Sci.* 120:1635–1645. https://doi.org/10.1242/jcs.001115

Sohrmann, M., C. Fankhauser, C. Brodbeck, and V. Simanis. 1996. The dmf1/mid1 gene is essential for correct positioning of the division septum in fission yeast. *Genes Dev.* 10:2707–2719. https://doi.org/10.1101/gad.10.21.2707

Stark, B.C., T.E. Sladewski, L.W. Pollard, and M. Lord. 2010. Tropomyosin and myosin-II cellular levels promote actomyosin ring assembly in fission yeast. *Mol. Biol. Cell.* 21:989–1000. https://doi.org/10.1091/mbc.e09-10-0852

Sun, L., R. Guan, I.J. Lee, Y. Liu, M. Chen, J. Wang, J.Q. Wu, and Z. Chen. 2015. Mechanistic insights into the anchorage of the contractile ring by anillin and Mid1. *Dev. Cell.* 33:413–426. https://doi.org/10.1016/j.devcel.2015.03.003

Swulius, M.T., L.T. Nguyen, M.S. Ladinsky, D.R. Ortega, S. Aich, M. Mishra, and G.J. Jensen. 2018. Structure of the fission yeast actomyosin ring during constriction. *Proc. Natl. Acad. Sci. USA.* 115:E1455–E1464. https://doi.org/10.1073/pnas.1711218115

Tao, E.Y., M. Calvert, and M.K. Balasubramanian. 2014. Rewiring Mid1p-independent medial division in fission yeast. *Curr. Biol.* 24:2181–2188. https://doi.org/10.1016/j.cub.2014.07.074

Vavylonis, D., J.Q. Wu, S. Hao, B. O'Shaughnessy, and T.D. Pollard. 2008. Assembly mechanism of the contractile ring for cytokinesis by fission yeast. *Science.* 319:97–100. https://doi.org/10.1126/science.1151086

Willet, A.H., N.A. McDonald, K.A. Bohnert, M.A. Baird, J.R. Allen, M.W. Davidson, and K.L. Gould. 2015. The F-BAR Cdc15 promotes contractile ring formation through the direct recruitment of the formin Cdc12. *J. Cell Biol.* 208:391–399. https://doi.org/10.1083/jcb.201411097

Wu, J.Q., and T.D. Pollard. 2005. Counting cytokinesis proteins globally and locally in fission yeast. *Science.* 310:310–314. https://doi.org/10.1126/science.1113230

Wu, J.Q., J.R. Kuhn, D.R. Kovar, and T.D. Pollard. 2003. Spatial and temporal pathway for assembly and constriction of the contractile ring in fission yeast cytokinesis. *Dev. Cell.* 5:723–734. https://doi.org/10.1016/S1534-5807(03)00324-1

Wu, J.Q., V. Sirotkin, D.R. Kovar, M. Lord, C.C. Beltzner, J.R. Kuhn, and T.D. Pollard. 2006. Assembly of the cytokinetic contractile ring from a broad band of nodes in fission yeast. *J. Cell Biol.* 174:391–402. https://doi.org/10.1083/jcb.200602032

Wu, J.Q., C.D. McCormick, and T.D. Pollard. 2008. Chapter 9: Counting proteins in living cells by quantitative fluorescence microscopy with internal standards. *Methods Cell Biol.* 89:253–273. https://doi.org/10.1016/S0091-679X(08)00609-2

Zhang, M., H. Chang, Y. Zhang, J. Yu, L. Wu, W. Ji, J. Chen, B. Liu, J. Lu, Y. Liu, et al. 2012. Rational design of true monomeric and bright photoactivatable fluorescent proteins. *Nat. Methods.* 9:727–729. https://doi.org/10.1038/nmeth.2021

Supplemental material

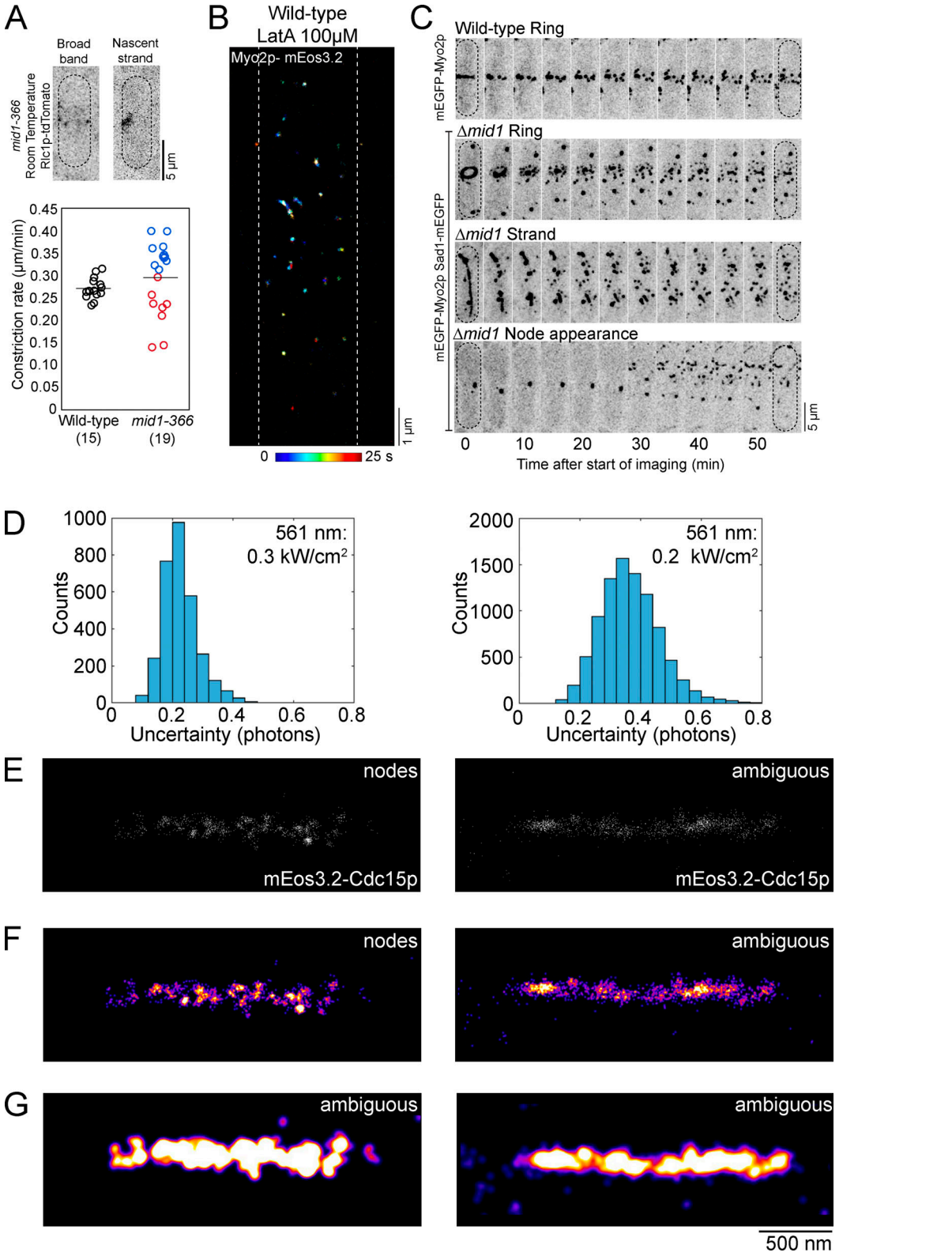

Figure S1. **P-nodes assemble in the absence of actin filaments. (A)** Swarm plot of the constriction rate for individual cells (bar, mean). Close-ups of *mid1-366* cells with a band of P-nodes (left) or a nascent strand (right). Number of cells counted in brackets. Blue circles, nascent strands. Red circles, enduring strands. **(B)** SMLM image of a wild-type cell expressing Myo2p-mEos3.2 treated with LatA. **(C)** Time series of micrographs of cells imaged after the addition of LatA. Dotted lines outline the cell perimeter. **(D)** Histograms of the positional uncertainty of the localized emitters. Top right corner: Measured power density of the 561-nm laser. **(E)** Cropped image of the localized emitters in the contractile rings of cells acquired with either a higher (left) or lower (right) 561-nm laser power density. **(F)** The contractile rings from D with a Gaussian kernel of σ 1.5-pixel applied, visualized with the fire colormap. **(G)** The contractile rings from D with a Gaussian kernel of σ 6-pixel.

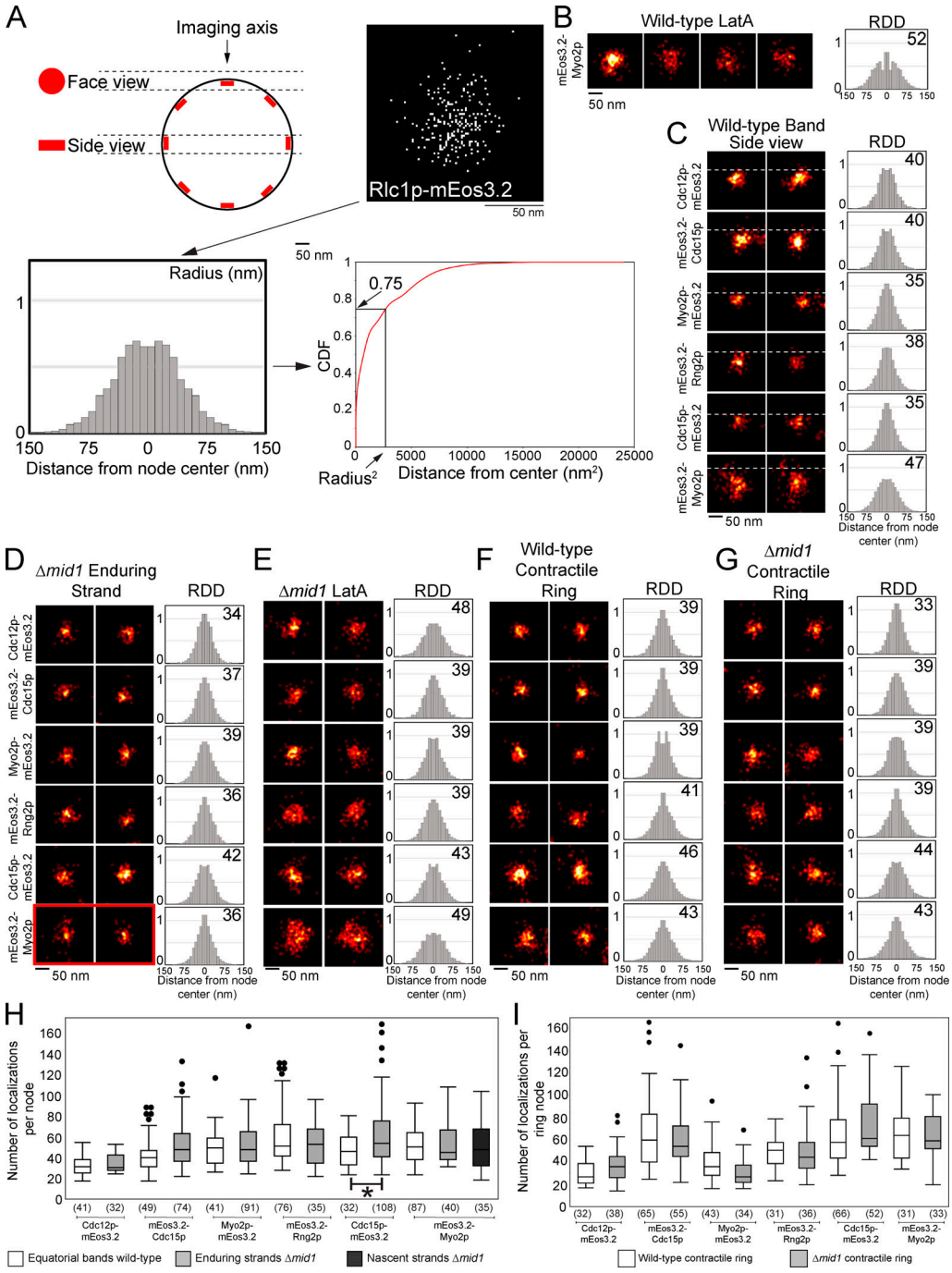

Figure S2. **Molecular organization of node proteins. (A)** Diagram of a cross-section of a fission yeast cell showing the imaging focal plane obtained by focusing on the surface and across the middle of the cell (top left). Image of localized emitters in a Rlc1p wild-type P-node (top right). Radial density distribution of the distance of localized emitters from the center of the node (bottom left). The cumulative distribution function of localized emitters as a function of the squared distance from the node center. The node radius represents the distance away from the center of the node that contains 75% of all localized emitters. **(B)** SMLM images of face views of mEos3.2-Myo2p in the P-nodes of LatA wild-type treated cells. **(C)** SMLM images of side views of P-nodes of wild-type cells labeled with six different mEos3.2 fusion proteins. Horizontal dotted line in side view indicates the edge of the cell. **(D and E)** SMLM images of face views of six different mEos3.2 fusion proteins in the P-nodes of *Δmid1* enduring strands and LatA-treated *Δmid1* cells. **(F and G)** SMLM images and RDD plots of R-nodes of wild-type (E) and *Δmid1* (F) cells acquired in face view and labeled with six different cytokinesis proteins fused to mEos3.2. The 50-nm scale bar applies to all SMLM node images. **(H)** Boxplot of the number of localizations per P-node in six different mEos3.2 fusion proteins. **(I)** Boxplot of the number of localizations per R-node in six different cytokinesis proteins labeled with mEos3.2 in wild-type and *Δmid1* cells. Statistical significance determined by ANOVA with Tukey's HSD; *, $P < 0.05$. Data distribution was assumed to be normal, but this was not formally tested. We noticed an unexpected difference in the number of localized emitters between the tip of the Myo2p tails and the heads in the R-nodes but not in the P-nodes (I). This difference is consistent between the two genotypes. All pairwise comparisons between wild-type and *Δmid1* structures for each protein in the boxplots were not significant, except when indicated (asterisk). Number of cells counted in brackets. RDD, radial density distribution. Whiskers in H and I are defined in Materials and methods. HSD, honestly significant difference.

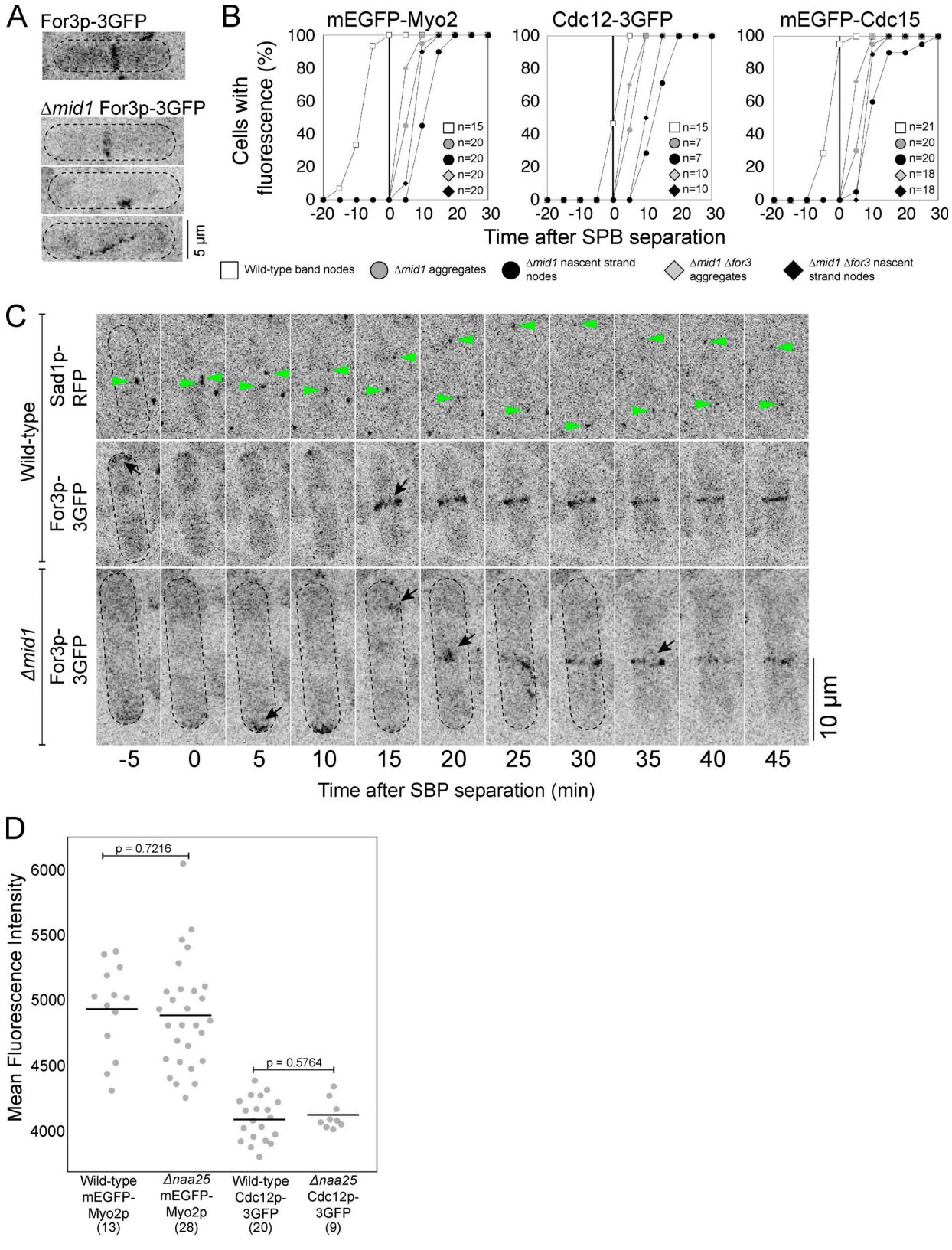

Figure S3. **Localization and timing of For3p recruitment. (A)** Confocal micrographs of wild-type or *Δmid1* cells expressing For3p-3GFP. **(B)** Outcomes plot of the accumulation of cytokinesis proteins in the P-nodes of the equatorial band or nascent strands or in aggregates at the poles of the cells in the cell population over time. **(C)** Time series of micrographs of wild-type (top) and *Δmid1* cells (bottom) expressing For3p-3GFP and Sad1p-RFP. Green arrowheads, SPBs. Black arrows, For3p-3GFP. **(D)** Swarm plot of the mean fluorescence intensity value per contractile ring for individual cells (bar, mean). Statistical significance determined by two-sided Student's *t* test; $P < 0.05$. Data distribution was assumed to be normal, but this was not formally tested. RFP, red fluorescent protein.

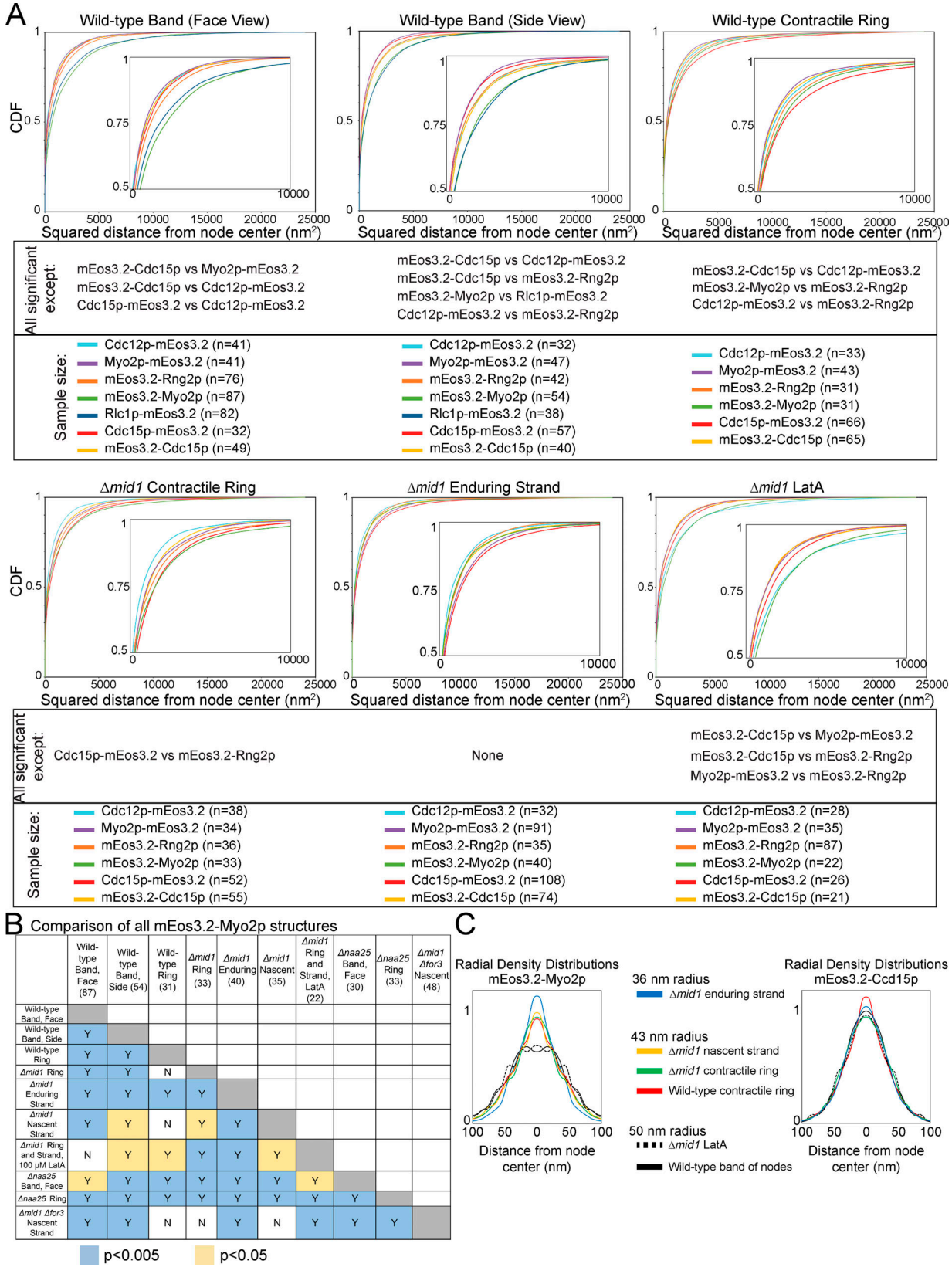

Figure S4. **Comparison of protein organization of cytokinesis proteins in the node. (A)** Plots of the CDF for each cytokinesis proteins in the band of P-nodes, strand P-nodes, and R-nodes. Inset, close-up of CDF curves. Non-significant pairwise KS tests at $P < 0.05$ are listed below respective CDF plots. **(B)** KS tests to determine whether the distribution of localizations was significantly different between pairs of node proteins within a structure. Yes (Y), significant difference at $P < 0.005$ (blue) or $P < 0.05$ (yellow). No (N), not significantly different. Number of nodes per marker are in brackets. **(C)** Overlaid radial density distribution plots of face views of mEos3.2-Myo2p and mEos3.2-Cdc15p in P-nodes and R-nodes.

Table S1 is provided online as separate Excel file. Table S1 lists the *S. pombe* strains described in this study.